



Huang, Rui (2022) *Overview of low molecular weight gel research and the effect of charge screening of wormlike micelles on the mechanical properties of gel noodles*. MSc(R) thesis.

<https://theses.gla.ac.uk/83356/>

Copyright and moral rights for this work are retained by the author

A copy can be downloaded for personal non-commercial research or study, without prior permission or charge

This work cannot be reproduced or quoted extensively from without first obtaining permission from the author

The content must not be changed in any way or sold commercially in any format or medium without the formal permission of the author

When referring to this work, full bibliographic details including the author, title, awarding institution and date of the thesis must be given

Enlighten: Theses

<https://theses.gla.ac.uk/>
research-enlighten@glasgow.ac.uk



University
of Glasgow

**Overview of Low Molecular Weight Gel
Research and the Effect of Charge Screening of
Wormlike Micelles on the Mechanical Properties
of Gel Noodles**

Rui Huang

Prof. Dave J. Adams

2022 Msc(R) Master's degree dissertation

School of Chemistry

College of Science and Engineering

23/09/2022

Acknowledgements

My deepest gratitude goes first and foremost to Professor Dave J. Adams, my supervisor, not only for his constant encouragement and guidance, but also provided me with 1ThNapFF, the key dipeptide for the project. He has walked me through all the stages of the writing of this thesis. Without his consistent and illuminating instruction, this thesis could not have reached its present form.

Second, I would like to express my heartfelt gratitude to Dr Daniel McDowall, who led me into this project and helped me to complete the small angle scattering part of the experimental study. I am also very grateful to Dr Henry Ng for his software support and thanks to Professor Louise C. Serpell and Dr Youssra K. Al-Hilaly for providing me with transmission electron microscopy (TEM) experimental data. Meanwhile, I would like to express my heartfelt thanks to the other members of the project team for their tireless training and discussions on professional issues during the year.

Last, my thanks go to my beloved family for their loving considerations and great confidence in me all through these years. I also owe my sincere gratitude to my friends and my fellow classmates who gave me their help and time in listening to me and helping me work out my problems during the difficult course of the thesis.

Abstract

Functionalised dipeptides that self-assemble at high pH to form worm-like micellar solutions can possess surfactant-like properties. By varying the salt concentration, the self-assembled structures and interactions between them change, resulting in solutions with very different shear and tensile viscosities. As a result, gel noodles with different mechanical properties and arrangements can be prepared from these precursor solutions.

TABLE OF CONTENTS

Acknowledgements	2
Abstract	3
List of abbreviations	5
1. Introduction	6
1.1 Low-Molecular-Weight-Gels	6
1.1.1. Properties of Low Molecular Weight Gels	7
1.2 Dipeptide-based Low-Molecular-Weight-Gelators	8
1.3 Peptide amphiphiles and other LMWG	10
1.4 Techniques to probe Low-Molecular-Weight-Gels	11
1.4.1. Method of determining gel formation	11
1.4.2 Phase transition temperature determination methods	12
1.4.3 Scanning electron microscope	12
1.4.4 Transmission electron microscopy	13
1.4.5 Atomic Force Microscopy	13
1.4.6 Small-angle scattering	13
1.4.7 UV-Vis spectrophotometry	14
1.4.8 X-ray diffraction experiments	14
1.4.9 Fourier transform infrared spectroscopy	14
1.4.10 Contact angle	15
1.4.11 Dripping-onto-substrate	15
1.5 Gel Noodles	16
1.6 Surfactants	20
1.7 Overview of Low Molecular Weight Gel Research and the Effect of Charge Screening of Wormlike Micelles on the Mechanical Properties of Gel Noodles	22
2. Experimental Details	23
2.1 Materials	23
2.2 Sample preparation	23
2.3 Dripping-onto-substrate	23
2.4 Shear and oscillatory rheology	25
2.5 Microscopy	26
2.6 Small angle scattering	27
2.6.1 Small angle neutron scattering (SANS)	27
2.6.2 Small angle X-ray scattering (SAXS)	27
2.6.3 Model fitting	27
2.7 Hydrogel noodle formation, bridging and dry filament formation	28
3. Results and discussion	29
3.1 Gel formation	29
3.2 Rheological properties	30
3.3 Dripping-onto-substrate results	34
3.4 Small angle scattering	41
3.5 Microscopy data	47
3.6 Bridge load test	53
4. Conclusions	54
5. References	55

List of abbreviations

AFM	atomic force microscopy
CPOM	cross polariser optical microscopy
DA	peptide-internal diacetylenes
DoS	dripping-onto-substrate
DSC	differential scanning calorimetry
EDX	energy disperse X-ray
EDS	energy dispersive spectrometer
FT-IR	fourier transform infrared spectroscopy
G'	storage modulus
G''	loss modulus
LMWG	low-molecular-weight gelator
PAM	polyacrylamide
PDA	peptide-polydiacetylene
POM	polarised optical microscopy
SANS	small-angle neutron scattering
SAXS	small-angle X-ray scattering
SEM	scanning electron microscope
SLD	scattering length density
TBAOH	tetrabutylammonium hydroxide
TEM	Transmission electron microscopy
UV-vis	Ultraviolet-visible absorption spectroscopy
WLM	worm-like micelles
XRD	X-Ray diffraction

1. Introduction

Advanced self-assembled nanomaterials have been widely used in biomedical science, information technology and environmental science.¹ Molecular self-assembling systems are currently a subject of great interest to the scientific community. Molecular self-assembly is driven by supramolecular interactions (for example, ionic, hydrophobic, van der Waals, hydrogen, and coordination bonds), but kinetically stable covalent bonds can also be involved.² Combined with their inherent fluidity, self-assembled systems can yield ordered nanostructures that have many interesting properties, such as error correction, self-healing, and a high sensitivity to external stimuli. Self-assembly refers to a technology in which spontaneous reactions occur between molecular-level or smaller structural units to form an ordered structure. During the reaction process, the basic structural units spontaneously form an internally stable structure with a certain regular appearance through the action of non-covalent bonds. A major feature of self-assembly is that the reaction has a certain controllability.³ Using self-assembled nanomaterials can introduce and tune a broad range of functional properties through finely tuned structural features.

1.1 Low-Molecular-Weight-Gels

Low-molecular-weight gels form a class of interesting materials that are widely used in industry and cutting-edge science.⁴ Jones et al. defined low-molecular-weight gels as a liquid encapsulated in a solid network consisting of fibrous aggregates small molecules.⁵ The unique properties and structures of low-molecular-weight gels have attracted extensive attention for decades. Low-molecular-weight gelators (LMWGs) based on non-covalent interactions endow low-molecular-weight gels with specific properties, such as reversibility. For example, it is common to control a gel to solution reversal by changing the temperature.⁶ As the temperature increases, the gel can be converted to solution and conversely, by lowering the temperature, and the solution can be converted to gel. Other interesting properties include responsiveness to external stimuli, and self-healing properties. The self-assembly behaviour of LMWGs has also attracted widespread interest among researchers. LMWGs have been used in fields such as medicine and agriculture due to their excellent biocompatibility and biodegradability.⁷ The formation of gels often revolves around the entanglement and cross-linking of a large number of fibres in their high-concentration solutions. LMWGs can be reversed by external energy transfer, such as heat and pressure. This property is very different from gels formed by permanent covalent bonds.^{5, 8, 9} The general process of low molecular weight gel self-assembly is shown in Figure 1: the LMWG is heated in an appropriate solvent, and the resulting supersaturated solution is cooled to room temperature. As the solution temperature decreases, the molecules begin to aggregate, and three different situations can occur: (1) crystals resulting from highly ordered aggregates; (2) random aggregates into amorphous precipitates; (3) somewhere

between the two states where a gel can be produced.⁶

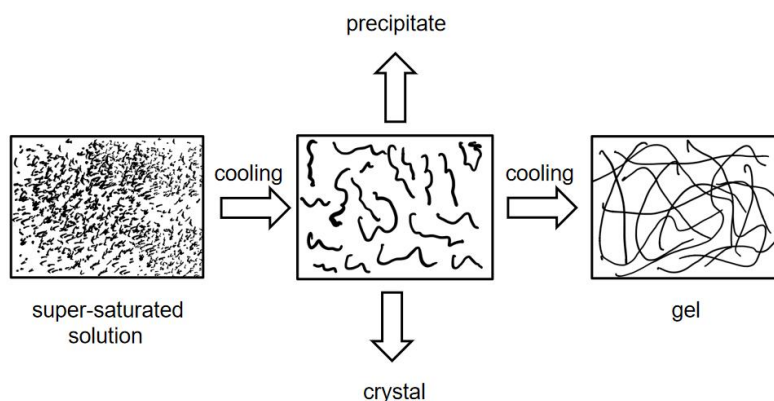


Figure 1. Schematic representation of the gel-process aggregation model. Triggers other than temperature can be used but cooling is shown in this example.

1.1.1. Properties of Low Molecular Weight Gels

The gel matrix is formed when the LMWGs form long fibrous structures by self-assembly within a solution that become entangled with each other. Gels with a range of different properties can be formed, for example with the ability to heal itself after being disrupted can have a significant impact on drug transport and cell culture. Chen et al. stated that the mechanical properties of low-molecular-weight gels will be influenced by the method by which the gel is prepared.¹⁰ The environment in which LMWG is self-assembled from the same raw material and the choice of triggering agent will affect the rate of self-assembly and the degree of entanglement of the internal fibres, thus affecting the mechanical properties. Gels are formed by dissolving or dispersing sample solute molecules and then adding a trigger to the prequel solution. Even the solid form of the same gel may be different, and different polymorphs may have different solubility, etc. The triggering agent directly affects the chemical and mechanical properties of the gel.¹¹ The differences in mechanical properties come from three different directions. They are (1) the average size of the fibres, (2) the distance between each crosslinking point inside the gel and (3) the length range distribution of the fibres.¹⁰

The network within the gel is susceptible to external factors that can lead to reversible changes in the gel. For example, Wezenberg et al. showed that gels formed from 2-vinylthiophene require high-temperature conditions (105-110°C) to induce the inverse gel-to-sol transition by photoswitching.¹² On the basis of this, a photoresponsive biuret LMWG was developed to better achieve the reversibility of the gel. They found that intermolecular hydrogen-bonding forces within an overcrowded olefinic biurea LMWG can be altered according to the wavelength of the irradiated UV light, resulting in trans-cis stilbene-type isomerization of the overcrowded olefinic biurea (Figure 2).¹² Some reports highlight that gel structure can change with time, after resting, or after different temperature treatments. As an example, under certain conditions, a change in

pH or a difference in the type of trigger agent can lead to a gel-to-crystal transition, with the molecules of the gelators crystallising directly from the interior of the gel.¹³⁻¹⁵ Over time, the initial gel formed in a network of gel systems may become more homogeneous over time, with the finer fibres forming a more stable structure than the coarser ones, resulting in a stronger gel. A recent study of gel-gel transitions is the transition from opaque to transparent dipeptide gels triggered by inorganic salt-like triggers.¹⁶

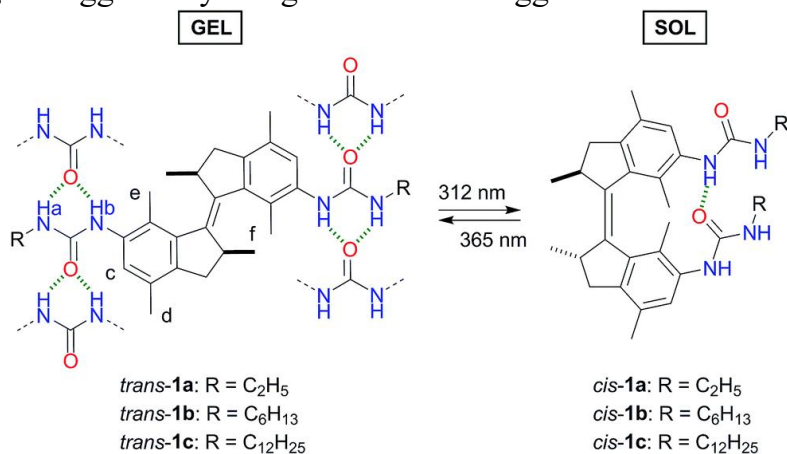


Figure 2. Photoisomerization behaviour of trans- and cis-bisurea LMWGs and urea hydrogen-bonding patterns.¹² Reproduced from S. J. Wezenberg, C. M. Croisetu, M. C. A. Stuart and B. L. Feringa, *Chem. Sci.*, 2016, 7, 4341, with permission from the Royal Society of Chemistry.

1.2 Dipeptide-based Low-Molecular-Weight-Gelators

According to several studies, there are many types of compounds that can be effective LMWGs.¹⁷ Currently, it is common to use a change in pH to induce gelation, which results in different degrees of dispersion of the same sample molecule in water at different pH values. This means that the sample will self-assemble to varying degrees at both pH values but will form a different structure. However, the gelator will never be completely soluble.¹⁸ Functionalised dipeptides can be effective LMWGs, and many functionalised dipeptides can be used as a switch to form gels using a change in pH.¹⁹ Dipeptide solutions are usually prepared at pH > 10, resulting in a micellar dispersion system by deprotonation of the terminal carboxylic acid (an example dipeptide LMWG is shown in Figure 3).¹⁹⁻²⁵

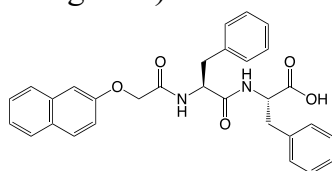


Figure 3. Chemical structure of 2NapFF.

There are several gelators available that are chiral, and one effective class of LMWG is a dipeptide functionalised with a series of aromatic moieties. For example, Yang et al. reported naphthalene dipeptides that formed gels at reduced pH.²⁶ Both conformations of the compound were equally effective

LMWGs, but the racemic mixture failed to form a gel. The chirality of the amino acids was found to result in the formation of fibres that were similarly classified as either left-handed or right-handed. Wang et al. showed that the racemate of the substituted ring (Glu-Glu) could form gels and that these gels were able to have better self-healing properties than either isomer.²⁷ This type of gel is of unique research value. The most important aspect of these LMWGs is the terminal carboxylic acid group used to drive the gel for gelation. At high pH, the carboxylic acid salt causes effective dispersion of the molecule. At lower pH, protonation of the carboxylic acid leads to significantly lower solubility and possible gelation.²⁶ At high pH, micellar aggregates are formed.²⁸ Under conditions where the molecules are not extremely hydrophobic, these aggregates tend to be non-persistent spheres. In contrast, under conditions where the molecules are more hydrophobic, these aggregates are typically worm-like micelles (WLM) and, in most cases, form viscous solutions.^{28, 29} Gels can be formed by lowering the pH of both solutions so this suggests that self-assembly produces gels by either of two mechanisms depending on the initial aggregates. Chen et al. found that when pH is reduced, some dipeptides that do not form a viscous solution first need to undergo a transition from spherical micelles to worm-like structures before the internal worm-like fibres bind laterally and entangle to form a gel network.³⁰ This means that if the functionalised dipeptide is able to form a gel when the peptide sequence is non-chiral, a viscous solution needs to be formed first at a high pH. In contrast, dipeptides that form spherical micelles at high pH are completely different in that the dipeptide will complete the transition from spheres to worm-like structures directly before gelation occurs.³⁰

It is also common to trigger gel formation from a pre-gel solution at high pH by adding salt to screen the charges,³¹ using a pro-gelator with a cleavable,³² solubilising group, or generating the gelator in situ from suitable precursors through a chemical or enzymatic reaction.^{33, 34} McAulay et al. found that the micellar aggregates formed by dipeptide-based gelators at high pH changed with different alkali metal salt solutions, thus affecting their properties.³⁵ A variety of alkali metal salt solutions can deprotonate a functionalised dipeptide 2NapFF terminal carboxylic acid to achieve the transition from micellar aggregates to the gel state.³⁶ Experimental data show that the stiffness of the gels formed with various alkali metal cationic trigger solutions is significantly higher than that of organic cationic solutions of tetrabutylammonium hydroxide (TBAOH). The internal fibre diameters of the gels formed by the TBA cationic triggers were significantly smaller than those of the gels formed by the alkali metal cationic triggers. Among the gels with Na-2NapFF, Li-2NapFF, K-2NapFF, Cs-2NapFF and Rb-2NapFF cationic triggers, only two samples of Na-2NapFF and Li-2NapFF had significant overlapping phases in the storage modulus (G') and loss modulus (G''). While the value of G'' was consistently greater than G' only in the Cs-2NapFF sample, G' was consistently greater than G'' in the other samples.³⁵

1.3 Peptide amphiphiles and other LMWG

As other examples of LMWG, peptide amphiphiles consisting of amino acids and fatty acids were designed by Irwansyah et al.³⁷ amongst others. Experimental data from atomic force microscopy (AFM) show that peptide amphiphiles with valine, proline or glycine as linkers can self-assemble into nanofibrous structures with a scale of 100-200 nm. At the same time, they show that although the hydrophilic part of the gelator shares a positive charge, the amphiphilic peptide PA7 (Figure 4) is still able to self-assemble. This suggests that dipeptides can self-assemble on either positively or negatively charged dipeptides. This implies that the positively and negatively charged amphiphiles have similar self-assembly properties and that the amphiphiles also show potential as a LMWG.

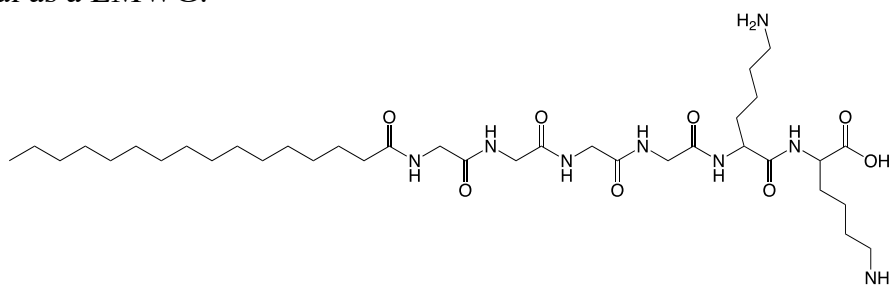


Figure 4. Chemical structure of PA7.

In 2022, Picci et al. synthesised three new bis-urea fluorescent low molecular weight gels (L1, L2, L3) based on tetraethyldiphenylmethane spacer groups, bearing indole, dansulfonyl and quinoline units as fluorescent fragments, as shown in Figure 5.³⁸ The anionic response of the gels was investigated. L1 forms gels in the polar solvent mixture DMSO/H₂O (15%v/v H₂O) and the dry gel scanning electron microscope (SEM) images show a dense fibrous network structure, which can come to investigate gel formation in the presence of anions of the third component. Weakly bound chloride does not inhibit the gelation process while binding to the relatively strong H₂PO₄⁻ delays gel formation but does not prevent gel formation after 24 hours, and binding to the very strong benzoate significantly hinders gel formation. The indole group in the molecule binds to the anion and regulates the fibril assembly process through the synergistic action of indole NH and urea NHs, thus controlling gel formation. In contrast, L2 and L3 form translucent gels in non-polar solvents such as chlorobenzene and nitrobenzene, and their dry gel SEM images show a thick fibrous entangled network. The unique stimulus responsiveness shows potential applications.

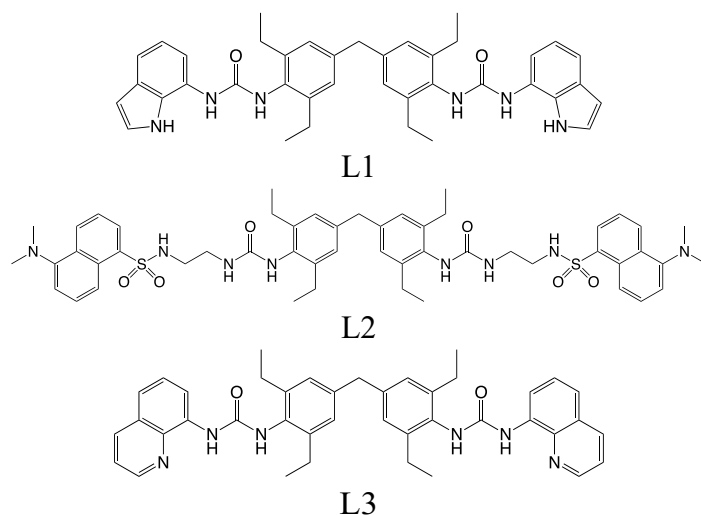


Figure 5. Biuret fluorescent LMWG L1, L2 and L3 based on tetraethyldiphenylmethane spacer groups.

1.4 Techniques to probe Low-Molecular-Weight-Gels

In recent years, research on low-molecular-weight gels has become more in-depth, and people have gradually increased the practical research tools for the study of LMWGs. This helps researchers in this field to explore the mysteries of low molecular weight gels more easily, quickly and effectively.

1.4.1. Method of determining gel formation

The formation of a viscous, non-flowing substance can be determined as a gel by using the "inverted vial" method and the rheometer method. The inverted vial method involves inverting the container containing the viscous immobile substance after stimulating the formation of the immobile substance, and after a while, if the system remains immobile, we can tentatively conclude that a gel has formed (Figure 6). In contrast, a rheometer can be used to test the magnitude of the storage modulus (G') and the loss of modulus (G'') of the substance. When the storage modulus $>$ the loss of modulus, we can state that the substance is a gel.³⁹

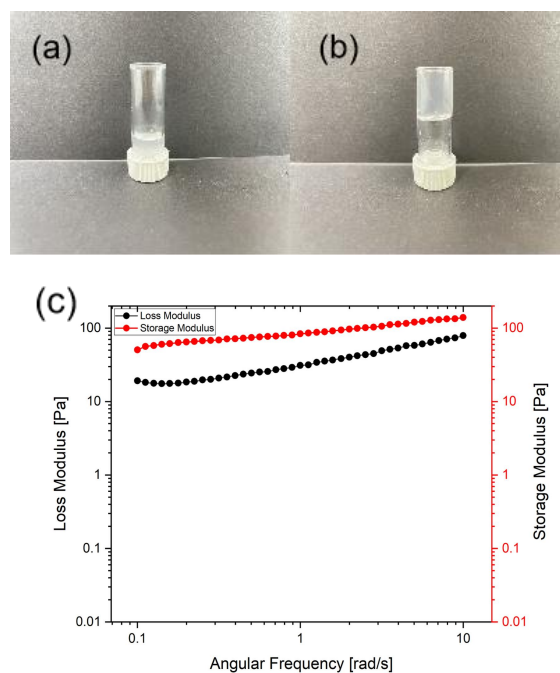


Figure 6. Non-gel (a) and gel (b) after inverting the vial for a period. (c) Example rheometer data from the author for gels showing example of storage modulus > loss modulus.

1.4.2 Phase transition temperature determination methods

The phase transition temperature of a gel can be measured by determining the differential scanning calorimetry (DSC) data for gel systems of different concentrations and measuring the transition temperature of the corresponding gel solute. DSC is a technique for measuring the power difference between a feed substance and a reference substance as a function of temperature at a programmed, controlled temperature.⁴⁰ It can be used to accurately measure the phase transition temperature of organic small molecule gels and the change in the heat of the gel system during the process. In addition to this, the thermodynamic parameters of the gelation can be calculated from the sol-gel phase transition diagram, allowing the thermal analysis of the phase state of the organogel system to be studied. A simpler method, the "falling ball method", is used to determine the phase transition state of a gel by observing the degree of falling of the balls when heated at a specific temperature.⁴¹ Rheology can also be used to determine the phase transition temperature by using a temperature ramp.

1.4.3 Scanning electron microscope

In the study of low molecular weight gels, the morphology leading to the formation of the gel is often observed by scanning electron microscopy (SEM). SEM is a more advanced means of microscopic observation than optical microscopy. SEM uses secondary electron signal imaging to observe the

surface morphology of the sample. SEM has a large magnification and a three-dimensional image and is a very effective and convenient way to observe surface morphology.

The samples need to be dried (often freeze-dried) during preparation as the organic reagents and solvents need to be removed. The surface morphology of the sample is therefore that of a dry gel.⁴² Experimental data from Mears et al. suggest that for LMWG studies, drying may lead to structural and morphological changes in the gel. In wet gels, the boundary of the fibre is defined by blurring, which is caused by the build-up of molecules within the fibre and the location of any remaining water molecules, whereas when the gel is dried, it has a more pronounced contrast.⁴³ Mears et al. also demonstrated that even after the pH of the LMWG had been reduced and the gel formed, some charge remained on the fibres. Further removal of the charge leads to fibre-fibre bonding and shrinkage of the gel phase, which is also associated with water. This means that the study of LWMGs after drying needs to be treated with caution.

1.4.4 Transmission electron microscopy

Transmission electron microscopy (TEM) is a higher resolution microscopic imaging tool than SEM. TEM is also able to penetrate the sample to observe its internal structure. Therefore, TEM is mainly used to observe the internal structure of self-assembled nanostructures within the gel. However, as for SEM, the sample preparation requires drying, so the observations are of dry gels. In recent years, cryo-TEM has been developed, which allows the direct vitrification of gel samples in liquid nitrogen to a solid state for observation, thus obtaining the closest possible approximation to the structure in the gel. This offers the possibility of a more accurate understanding of the structure of gels.⁴⁴

1.4.5 Atomic Force Microscopy

Atomic Force Microscopy (AFM) is a class of microscopy technique that use interatomic forces to study the surface properties and structure of matter. Of relevance to gels, no vacuum is required during the test and so, in contrast to SEM and TEM, AFM can allow in situ observation of the morphology of gels, which reduces the influence of the external environment on the morphology of the gel. This reduces the influence of the external environment on the morphology of the gel.³⁷

1.4.6 Small-angle scattering

Small-angle X-ray scattering (SAXS) and small-angle neutron scattering (SANS) are scattering techniques that allow data collection of nanoscale density differences in samples. This means that the structural organisation of gels can be further understood, and the characteristic distances of the assembly, alignment and mixing of ordered materials at the nanoscale condensed matter can be determined. SANS has a particular advantage over SAXS in that it has a

greater penetration depth and does not suffer from sample beam damage⁴⁵ but is typically much slower.

In synchrotron X-rays, electrons are radiated tangentially in a circular motion. Synchrotron X-rays are characterised by high brightness, high directivity and high monochromaticity, a higher signal-to-noise ratio and resolution can be achieved. Since the frequency, ω , of the X-rays is much higher than the intrinsic frequency of the electron vibration is ω_0 ($\omega \gg \omega_0$), this makes the scattered light still have the same wavelength as the incident light, but the phase is opposite, i.e. Thomson scattering occurs between the X-rays and the scatterer. If the angle between the incident light and the scattered light is 2θ , the scattering vector is defined as the difference between the incident light wave vector and the scattered light wave vector.

$$(1) q = \frac{4\pi}{\lambda} \sin 2\theta$$

In formula (1), λ is the scattering wavelength. If the scatterer, i.e. the electron density, is uniformly disordered in the material, then the scattered light will be uniformly distributed. For the materials where there is an inhomogeneous electron density, the scattered light in a particular direction carries structural information, and the microstructural parameters of the material can be obtained by analysing the light intensity of the scattered light in relation to the scattering vector.⁴⁶

1.4.7 UV-Vis spectrophotometry

When the self-assembly of low molecular weight gelling agent molecules occurs, the molecules interact by non-covalent interactions, and to probe the type of forces acting in a particular gel, spectroscopic techniques can be applied.

Ultraviolet-visible absorption spectroscopy (UV-vis) allows the absorption of ultraviolet and visible light by molecules to be determined. This provides a strong basis for the analysis of weak interactions between molecules of gels since aggregated molecules often have different absorption of light compared to non-aggregated molecules.⁴⁷

1.4.8 X-ray diffraction experiments

X-Ray diffraction (XRD) is the study of the internal composition, atomic or molecular structure and morphology of material by analysing its diffraction pattern. The information obtained from the pattern can be used to determine packing within gel fibres help to obtain possible configurations for the self-assembled stacking of gelling molecules.^{47, 48}

1.4.9 Fourier transform infrared spectroscopy

Fourier transform infrared spectroscopy (FT-IR) allows the analysis of substance identification based on the absorption of infrared light by molecules.

In the field of gels, this technique is mostly used to identify the hydrogen bonding between molecules upon self-assembly. By comparing the infrared spectra of free molecules with the infrared spectra of the gel structure, changes in the hydrogen bonding forces between molecules can be identified after gel formation.⁴⁹

1.4.10 Contact angle

The contact angle is the tangent line of the gas-liquid interface made at the intersection of the gas, liquid and solid phases through the liquid and the angle between the solid-liquid junction line is a measure of the degree of wetting. When the organic small molecule gel is formed into a membrane, the contact angle instrument can be used to characterise the films.⁵⁰

1.4.11 Dripping-onto-substrate

The DoS rheometer is a rheological instrument with an imaging unit and a fluid control system (Figure 8). DoS is an emerging technology for the study of LMWG. The dripping-onto-substrate (DoS) rheometry protocol is used to visualise the thinning and pinch-off kinetics of the slim neck formed between the droplet of a syringe needle and a fixed substrate over time (Figure 8), for measuring shear viscosity, power law index, tensile viscosity, relaxation time. The versatility of the DoS rheometer combined with MATLAB allows for the visualisation and dynamic analysis of particle-laden fluids. Such as polymer solutions, emulsions, worm-like micelle solutions etc. DoS rheometry provides one of the cheapest methods to measure the viscosity of Newtonian fluids and the relaxation time of polymer solutions.⁵¹

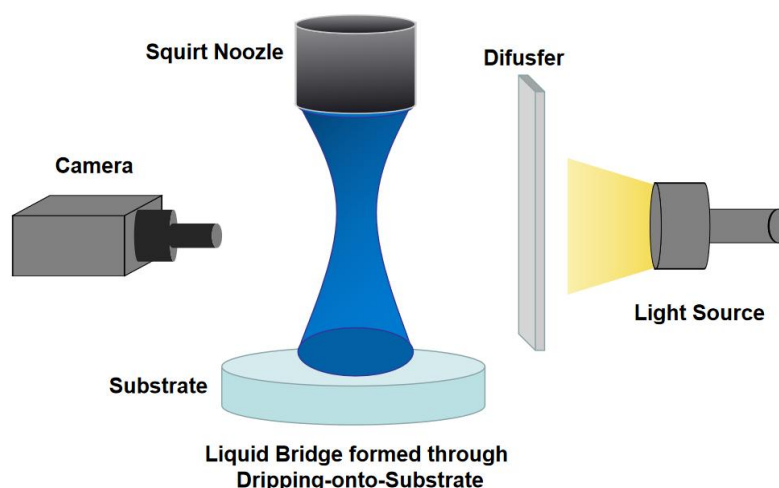


Figure 8. Dripping-onto-substrate (DoS) rheometer. The experimental setup consists of an imaging system that captures the dynamic changes of the sample, a light source, a diffuser and equipment with high-speed photography capabilities, and a liquid dispensing system that includes a syringe pump that can control the sample flow rate and a substrate adapted to the sample. The changes in neck shape and radius over time are then analysed frame by frame through MATLAB.

1.5 Gel Noodles

Many researchers have used a technique to make low-molecular-weight gel “noodles” by injecting small volumes of a precursor solution through a pipette or needle into inorganic salt solutions to form gel filaments, a method first reported by Zhang and his colleagues in 2010 using peptide amphiphiles in solution.⁵² This method of rapid preparation of low molecular weight gel noodles is practical and straightforward, but it has obvious limitations because most of the experimental manipulations are not controlled by the instrument, which makes it impossible to accurately measure the length and diameter of the gel noodles and reproduce the injection time and speed. Filament morphology and nanostructure alignment will depend on many factors, including injection flow rate, pipette/needle inner diameter, gel trigger medium, and how the injection is performed (e.g., static or dragged, Figure 9).^{53, 54}

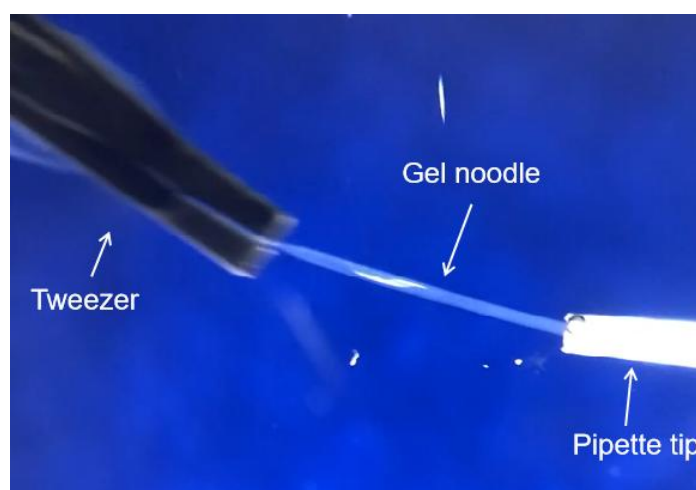


Figure 9. Using tweezers to drag a pre-gel solution from a pipette tip in a salt solution to form a gel noodle. Image collected by the author.

Zhang et al. discovered a thermal pathway that converts isotropic solutions containing peptide molecules into liquid crystals by hand pumping from a pipette into a salt solution to form single domain gels of aligned thin filaments, where the supramolecular structure of the self-assembled molecules changes significantly with the pathway.⁵² They found that it was possible to form noodle-like strings of arbitrary length by manually squeezing an aqueous peptide amphiphile solution from a pipette into a CaCl_2 solution, with uniform birefringence observed along the length of the line. This observation indicates that a macroscopic alignment extending over more than a centimetre was achieved. Using the same method, the unheated solution did not form mechanically stable string-like gels or show any birefringence. Zhang et al. showed that the gel noodle formed by the heated peptide amphiphiles solution contained very long arrays of well-aligned nanofibre bundles, but the unheated peptide amphiphiles solution formed a matrix of randomly entangled nanofibres. In contrast, simply dragging the unheated peptide amphiphiles solution did not

result in the formation of significantly neat nanofibre bundle arrays, and only the heated solution produced gel noodle that showed neat alignment.

Zhang et al.'s experiments in which the self-assembled nanofibers are formed are triggered by charged amino acid residues being crosslinked by the calcium salt. When calcium chloride was added to an amphiphilic peptide solution at different temperatures, the noodles formed from the heated solution phase gels were at least four times harder than those made from unheated solutions. Microscopically, gels formed from unheated solutions exhibited isotropy and no birefringence, whereas gels formed from heated solutions had large domains of birefringence (Figure 10).⁵²

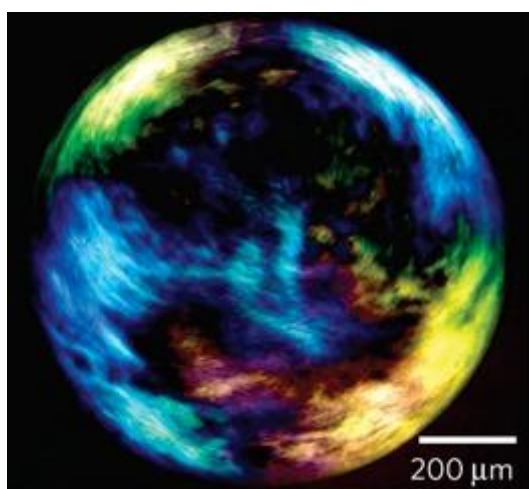
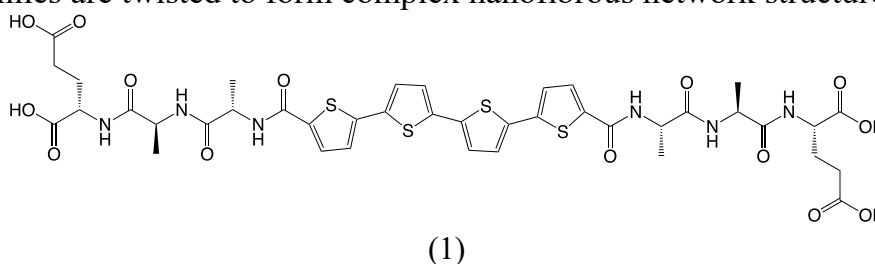


Figure 10. Birefringence domains between cross polarities of bubble gels.⁵² Reprinted with permission from Springer Nature, S. Zhang, M. A. Greenfield, A. Mata, L. C. Palmer, R. Bitton, J. R. Mantei, C. Aparicio, M. O. De La Cruz and S. I. Stupp, *Nature Materials*, 2010, 9, 594-601.

In the 'noodles' prepared by Tovar et al., two bolaamphiphilic peptides (Figure 11) were found to form strong, rigid self-supporting hydrogels after sonication, which allowed the gel noodles to be processed into more complex forms such as helical and nodular shapes. Hydrogen bonding interactions and π -stacking interactions predominate in the self-assembly process. This nanofibrous network structure is formed during the gel phase, in which these peptide amphiphiles are twisted to form complex nanofibrous network structures.⁵⁵



Stephen et al.⁵⁶ not only promote intertwined cross-linking of internal fibres upon self-assembly but also overcome unfavourable steric or tetragonal stacking within the nanostructure. The gel noodles they produced were also able to achieve macroscopically aligned π -conjugated nanostructures (Figure 13). In their peptide-polydiacetylene (PDA) randomly aligned nanostructure polymerisation process, a number of one-dimensional fibres also produced highly aligned conjugated polymer arrays.

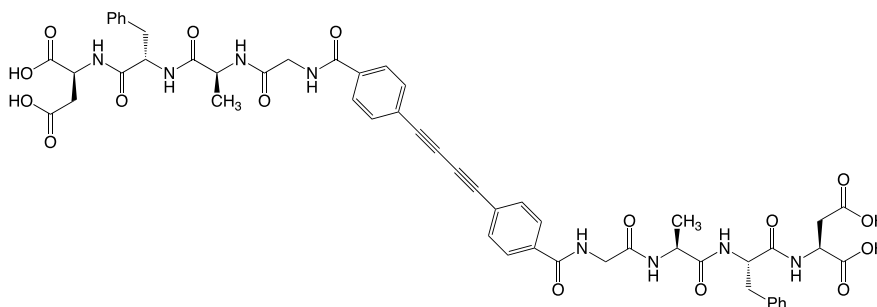


Figure 13. Structure of aromatic diacid peptide.

Polarised optical microscopy (POM) distinguishes the difference in birefringence before and after polymerisation by looking at the overall degree of alignment of the peptide-PDA spaghetti. They observed a red appearance in the gel noodles, but this was only the interaction of the nanostructures in the gel noodles with the polarised light, and this particular colour was not related to the resonance process. They also found that the peptide-internal diacetylenes (DA) noodles formed spatially resolved PDAs along the length of the peptide-DA noodles by using the TEM grid as a shadow mask during the photopolymerisation process and that different coloured birefringent regions were formed at locations with and without PDA formation under POM observation (Figure 14). They call this spatially-resolved polymerisation a 'micro-barcode', which can be used to measure the mechanical gradient of a gel spaghetti composed of macroscopically aligned conjugated polymers throughout. They also show that the alignment of the conjugated polymers can be easily obtained by extrusion without the influence of the physical 'director'.

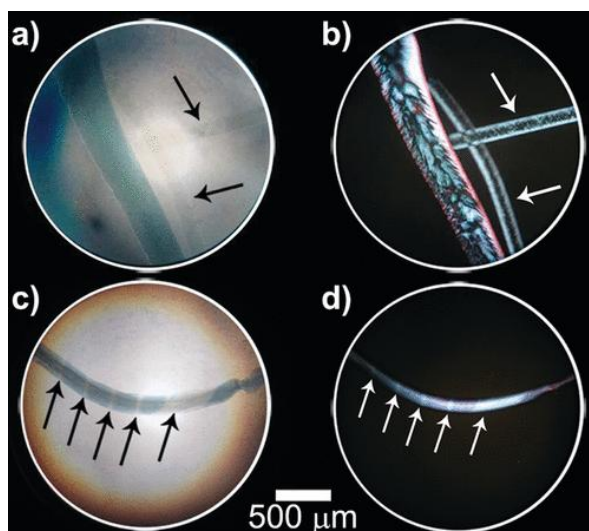


Figure 14. Colourless peptide hydrogel noodles before DA polymerization and blue peptide hydrogel noodles after polymerization are imaged under an optical microscope without (a) and with (b) crossed polarizers. Spatially controlled polymerization of peptide-DA noodles after gradient-shaded masking by TEM (c, d). Arrows indicate areas shielded from UV light.⁵⁶ Reproduced from S. R. Diegelmann, N. Hartman, N. Markovic and J. D. Tovar, *Journal of the American Chemical Society*, 2012, 134, 2028-2031., with permission from the American Chemical Society.

1.6 Surfactants

Conventional amphiphiles contain a polar head and one to two hydrophobic tails. The polar head can be a range of functional groups, including carboxylic acids, amino acids, sugars, phosphates or quaternary ammonium salts. Similarly, hydrophobic tails can be of many different types, depending on the number, length, flexibility, saturation, ring and so on. Such molecules are common in nature, such as lipids, and exist in many different aggregated states in aqueous solutions and hydrogels.⁵⁷

In an earlier report, Kunitake et al.⁵⁸ divided the amphiphilic structure into four separate parts: a flexible tail, a rigid segment, a spacer group and a hydrophilic head (as shown in Figure 15) and investigated possible aggregation forms (including spheres, vesicles, sheets, rods, tubes and discs). The structure of the aggregates can be changed by varying the length of the tail, the flexible connecting unit or both. They identified flexible tails, rigid segments and hydrophilic heads as essential elements for stable self-assembly.

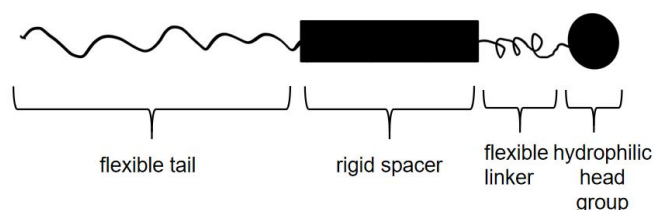


Figure 15. Schematic representation of conventional amphiphiles.

Bola-amphiphiles are amphiphilic molecules with two heads.⁵⁹ Similar to conventional amphiphiles, the aggregation properties can be modified by the chemical properties of the various head groups and linking groups, and by the formation of a variety of different aggregation forms. For example, they can form bilayers, followed by vesicles and other bilayers. They can also be folded in half and form micelles for different linkage lengths and flexibility, as shown in Figure 16.

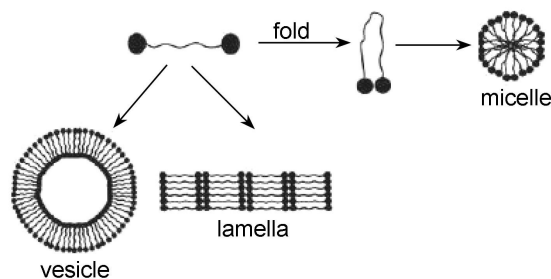


Figure 16. The different types of aggregates that can be formed by a bolaamphiphile.

Shimizu et al. studied a series of double-headed amphiphiles with different head groups,^{61, 62} including nucleosides,^{60, 61} amino acids and sugars, which can form both gels and fibres. The degree of aggregation of sugar derivatives is dependent on the parity of the alkyl carbon chain,⁶² demonstrating that the length and orientation of the alkyl chain linking the glucose groups at both ends has a strong influence on the aggregation of the molecule. The aggregation pattern of amino acid derivatives varies with pH due to the presence of carboxyl groups at the terminals, and the acidity coefficient pK_a varies with the length of the alkyl chain.⁶³ At high pH, the diglycopeptide derivative formed rod-like micelles (as observed by cryo-TEM); while at lower pH, protonation occurs on the surface of the micelle, causing aggregation between ionised and un-ionised individuals and then the formation of microtubules. Further increases in proton concentration protonate all residual carboxylates and lead to the precipitation of needle-like microcrystals. Compared to the dinucleoside-based double-headed molecules, the deoxyribose and phosphodiester-based gel factors are more complex and more soluble, allowing for good gel formation. The former can only form fibrous microcrystalline precipitates at shorter chain lengths and gels only at 20 carbon alkyl chains.⁶⁰

Of relevance to the work in this thesis, McDowall et al. identified a functionalised dipeptide 3-phenyl-2-[3-phenyl-2-[2-(5,6,7,8-tetrahydronaphthalen-1-yloxy) acetamido] propanamido] propanoic acid (1ThNapFF, Figure 17), 1ThNapFF that undergoes self-assembly into worm-like micelles under highly basic conditions to form further shear-thinning solutions.⁵³ Like many peptide-amphiphiles, 1ThNapFF forms gels with calcium salts with high mechanical strength.

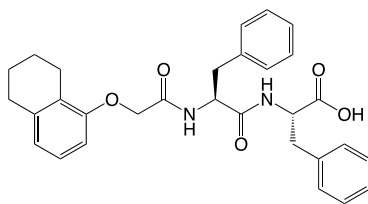


Figure 17. Chemical structure of 1ThNapFF.

1ThNapFF (Figure 17) forms WLM at high pH when the terminal carboxylic acid is deprotonated, which can be used to form well-defined noodles. Such molecules can broadly be regarded as surfactants. In this thesis, 1ThNapFF is considered a surfactant, and it is expected that the self-assembled structure will be influenced by the concentration of added salt, which will screen the charge and lead to a decrease in the critical micelle concentration, thus increasing the entanglement and interaction of the negatively charged WLM. By varying the salt concentration, the 1ThNapFF self-assembled structures and the interactions between them change, resulting in solutions with very different shear and tensile viscosities. As a result, gel noodles with different mechanical properties can be prepared. The mechanical strength of 1ThNapFF was later evaluated.

1.7 Overview of Low Molecular Weight Gel Research and the Effect of Charge Screening of Wormlike Micelles on the Mechanical Properties of Gel Noodles

Previous studies have investigated the conditions for the formation of 1ThNapFF low-molecular-weight-gel noodles and the minimum concentration of 1ThNapFF required for gel noodles. Studies on some LMWG noodles have shown that they are mechanically strong and can be spiralled or knotted, etc.⁵² In this thesis, the ultimate load-carrying capacity of gel noodles with different salt concentrations will be evaluated by means of bridge-loading experiments. Using common analytical techniques such as oscillatory rheometry, it is not possible to measure the mechanical properties of gel noodles for small and one-dimensional shaped samples. Previous data on the mechanical properties of LMWG are scarce. In 2021, McDowall et al. investigated nanoindentation of 1ThNapFF low molecular weight gel noodles that a technique that allows the mechanical properties to be measured at the micron level for localised areas of the measured material.^{53, 64} In this thesis, we will continue to further investigate the mechanical properties of 1ThNapFF gel noodles by exploring the extent to which the same molar equivalent of 1ThNapFF undergoes self-assembly in different molar equivalents of NaCl solutions. Meanwhile, the extent to which the shear-thinning solutions of 1ThNapFF under different molar equivalents of NaCl solutions have G' and G'' trends. Meanwhile, the microstructural differences between the shear-thinning solutions of 1ThNapFF under different molar equivalents of NaCl solution in normal and polarised light of the

microscope. The relaxation time (λ_E) and tensile viscosity of the different shear-thinning solutions were also measured with the technical support of DoS. Small-angle X-ray scattering (SAXS) and small-angle neutron scattering (SANS) measurements were also carried out on different samples by Daniel McDowall (University of Glasgow) and the results used here to explain the differences in the structure of WLM with NaCl. Meanwhile, the gel noodles produced after the salt bath treatment was dried and subjected to scanning electron microscopy to observe the difference in nanoscale structure.

2. Experimental Details

2.1 Materials

1ThNapFF was prepared by Professor Dave Adams using an established method.⁶⁵ Deionised water was used throughout. Sodium chloride, sodium hydroxide, calcium chloride, deuterium oxide and sodium deutroxide (40% w/v) were purchased from Sigma Aldrich and used as received. Solutions of sodium hydroxide were prepared directly from pellets to the required concentration.

2.2 Sample preparation

The 1ThNapFF solution was prepared by weighing 1ThNapFF (into a vial. The desired volume of deionised H₂O was added, followed by the desired volume of aqueous 0.5 mol/ L NaCl. The absolute amounts of H₂O and NaCl solution varied according to the amount of NaCl equivalent (eq.) required for this sample. Following this, NaOH was added to deprotonate 1ThNapFF. To avoid a pH overshoot and subsequent necessity to add of acid that would alter the final NaCl concentration, an insufficient amount of NaOH (0.8 equivalents) was first added using 2 mol/L NaOH aqueous solution. The solution was then stirred overnight, and the pH was adjusted to 11.3 by adding 2 mol / L and 0.1 mol / L NaOH (different concentrations were required depending on how much of a pH change was needed).

2.3 Dripping-onto-substrate

The drop-on-substrate (DoS) device was created by Daniel McDowall based on experience from previous studies.^{50, 66} This device and setup was optimised by the author. In order to record the thinning process, an iPhone 8 smartphone camera with a clip-on macro lens was used. In the small area where the DoS occurs, clip-on microscopes are ideal for high-quality imaging. For recording the process of filament breakage, there are two ways, slow motion (240 frames per second (fps) or standard (30 frames per second (fps) video function depends on the speed at which filament breaks. The contact line of the sessile droplet was held by a circular glass substrate of 4 mm diameter, thereby reducing the effects of wetting. Dispensing of the fluid was accomplished with a needle with

a 19 gauge flat tip attached to a 10 mL syringe. The Alaris CareFusion syringe pump controlled the rate at which fluid is dispensed. Three experiments (3 drops) were performed for each liquid after fixing the needle on the substrate using a distance of 4 mm for all experiments, and the thinning of each liquid was recorded.

As a method to reduce pre-shear, the plunger was drawn out of the back of the fluid first before the fluid was loaded into the syringe. Fluid was poured into the back of the nozzle after being sealed briefly with Blu-tac. As the plunger is returned to the syringe, the fluid is inverted so that it is above the air towards the plunger. Afterwards, any excess air was removed from the syringe. There is a need to remove the air in the syringe pump so that bubbles will not appear and inaccuracies will not occur in the flow rate because the air trapped in the pump will be compressed by the pump resulting in additional forces and pressures. There was a 5 mL/hr flow rate of fluid being dispensed slowly through the syringe until the first droplet appeared at the end of the syringe after the fluid was loaded into the syringe. To measure the amount of fluid dispensing per hour, we set the fluid dispensing rate to 0.2 mL/hr for the measurements. For fast thinning processes, this flow rate is slow enough to ensure that no impact is caused on the thinned liquid bridge in the process. In the case of slower thinning processes (more than 5 seconds), the flow must be stopped before the droplet makes contact with the substrate before the flow can continue. Once the syringe is stopped, the droplet continues to grow for a few seconds, and it can be timed so that it contacts the substrate during this period to ensure that it contacts the substrate while it continues to grow. As a result of pressing the button, vibrations are created throughout the setup, and thus the flow cannot be stopped during the thinning process.

It is by default that video recordings on the iPhone are saved as .mov files, and necessary to convert the videos into individual frame-by-frame .tiff files in order to perform the image analysis. This conversion process involves several steps, each of which requires a different kind of software for each of them.

1. VLC media player (version 3.0.12) converts .mov to .mp4.

An in-built tool within the VLC media software was used to convert the .mov files to .mp4 files.

2. FFmpeg (2021-04-04 build) converts .mp4 to .avi.

In order to convert the .mp4 files to the uncompressed .tiff files, they were first converted to the .avi file format using FFmpeg using the following command line, “ffmpeg -i filename.mp4 -pix_fmt nv12 -f avi -vcodec rawvideo convertedFile.avi”

3. ImageJ (version 1.52n) converts .avi to .tiff.

Using ImageJ, the .avi files were then opened and saved as an "Image

Sequence" in a dedicated folder for that particular video. A folder of .tiff files showing each frame of the process was created as a result of this process.

To extract the evolution of filament diameter over time from the .tiff files, the 'canny edge' detection system was used in MatLab (version R2021a) in order to process the .tiff files. A slender filament was measured at its halfway point along its length after it had been formed and the radius of the filament was calculated. For each experiment, the pixels/mm value was calibrated by comparing the outer diameter of the 19G needle to a scale bar to help determine the pixels/mm value.

In the initial stages of droplet contact and thinning, a variety of factors must be taken into consideration, including surface tension, viscosity, and inertial forces.⁶⁷ In the later stages of the process, a thin filament forms, which is thinned and breaks at the end of the process. We have determined that the slender filament is to have been formed when the filament height is ten times the filament diameter that we are investigating in this thesis.⁶⁸ There is a regime known as the elastocapillary regime, which has been described previously by Entov and Hinch (equation 2).⁶⁹

$$(2) \quad \frac{R}{R_0} = \left(\frac{G_E R_0}{2\sigma} \right)^{\frac{1}{3}} \exp\left(-\frac{t}{3\lambda_E}\right)$$

where G_E is the elastic modulus, λ_E the extensional relaxation time, R_0 radius of the dispensing needle, R filament radius and σ the surface tension. Therefore, to fit the thinning of the slender filament to an exponential decay curve to determine the extensional relaxation time (λ_E). In Origin 2020 software, a calculation is performed to determine the fit of the data using the "ExpDec1" equation, which can be seen in equation (3). The slender filament was detected by analysing the frames in ImageJ and determining the exact time when it formed.

$$(3) \quad y = A1 \exp\left(-\frac{x}{t1}\right) + y0$$

Because there was no measurement of the surface tension of these fluids, it is not possible to calculate the G_E of these fluids.

2.4 Shear and oscillatory rheology

In this study, shear and oscillatory rheology measurements were carried out using a Physica 101 rheometer from Anton Paar. The geometry for determining the shear viscosity of the material used in this study was a cone and plate of 50 mm diameter. This measurement was carried out at a controlled temperature of 25°C that was fixed for the duration of the experiment. A thin layer of solution

was poured onto a plate to reduce preshear and to allow the measurement to be conducted. The shear rates ranging from 1 - 100 s⁻¹ was investigated. We performed three repeat measurements for each solution and calculated the average viscosity for each shear rate according to the results of the three repeat measurements.

A cup and vane geometry were used for the oscillatory frequency sweeps. The frequency range of the studied oscillatory strain was between 1 - 100 Hz with a fixed oscillatory strain of 1 %. At each NaCl concentration, 3 x 2 mL solutions in Sterilin vials were prepared and measured in terms of their concentration. Averaging the 3 repeat solutions at each NaCl equivalent was carried out.

2.5 Microscopy

The images were collected using a Nikon Eclipse LV100 optical microscope with an Infinity 2 camera that was used to capture images from the microscope. A transmission microscope was used in this study to collect images. The images were generally collected under both normal white and cross-polarised light, with both being used concurrently.

The 1ThNapFF solutions were measured on a microscope slide as a pool of solution so that the images could be seen clearly. Using a cut Pasteur pipette, the liquid was transferred to the slide. The pipette was cut to reduce shear during dispensing.

As a preventative measure, gel noodles were analysed on microscope slides in a solution containing 50 mM CaCl₂ to prevent drying.

The SEM morphology of the sample filaments was evaluated using an FEI XL30 ESEM microscope. Vacuum-dry the measured sample filaments and fix them on a nail-shaped sample stage to prepare samples by gold-plating on a Polaron SC7640 automatic/manual high-resolution sputtering coater. And observe and collect SEM images at 100X, 500X, 1kX, and 2kX magnifications.

EDX microanalysis was performed on selected samples using The Oxford Instruments Energy 250 energy dispersive spectrometer system (EDS). Image recording is via a SONY video graphics printer or digital by processing image frames in a 16 bit framestore computer for output to hard drive, USB flash drive or CD writer.

TEM images were collected by Youssra Al-Hilaly (University of Sussex). 4 μL of each sample was placed onto formvar/carbon-coated 400-mesh copper grids (Agar Scientific). The grids were washed twice with 0.22-μm-filtered milli-Q water, followed by the addition of uranyl acetate (2% w/v; 4 μL). The grid was left for 30 seconds before blotting and air-drying. TEM projection images were collected using a JEOL JEM1400-Plus Transmission Electron Microscope operated at 80 kV equipped with a Gatan OneView camera (4k × 4k). Images

were recorded at 25 fps with drift correction using GMS3.

2.6 Small angle scattering

All small angle scattering measurements were carried out by Daniel McDowall (University of Glasgow) at Diamond Light Source or Lisa Thomson (University of Glasgow) at Rutherford Appleton Laboratory. The data were fitted by Daniel McDowall.

2.6.1 Small angle neutron scattering (SANS)

The SANS measurements were carried out at the Rutherford Appleton Laboratory (Didcot, U.K.) using a sample changer and water bath at 25 °C Celsius on the ZOOM beamline of the ISIS pulsed neutron source. This instrument was operated in pinhole collimation, with the distance between source and sample and the distance between sample and detector set to $L1 = L2 = 4\text{ m}$. This gave scattering vector (q) range of 0.004–0.722 \AA^{-1} where $q = 4\pi/\lambda\sin(\theta/2)$ using neutrons of wavelengths (λ) 1.75–16.5 \AA by the time-of-flight technique. The data was reduced using MantidPlot and the SANS curves were fitted using SasView (version 5.0.2) after the data reduction was completed. A D₂O background and 1ThNapFF solutions were measured in UV spectrophotometer grade quartz cuvettes (Hellma), which have 2 mm path lengths. The I vs q plots were obtained by azimuthally integrating the scattering patterns in 2D. The scattering for the D₂O background was subtracted from the 1ThNapFF solutions.

2.6.2 Small angle X-ray scattering (SAXS)

Using a 1 mL syringe and a 21G needle, samples were loaded into 1.5 mm diameter polycarbonate capillaries. The capillaries were sealed with a plug of polycarbonate extrusion and then epoxy resin to prevent any drying/sample loss in the vacuum chamber.

SAXS was performed at Diamond Light Source on the offline Xenocs 3.0 instrument that was used to perform SAXS measurements. An X-ray source with an energy of 9.24 keV based on gallium and indium metal jets. At a detector distance of 1.5 m, scattering measurements were conducted with a q range of 0.0055 to 0.29 \AA^{-1} . The data was collected for a period of 10 minutes.

Dawn Science (version 2.23.0) was used to process the scattering data. The scattering from water was used as the background and subtracted from samples. We performed an azimuthal integration of 2D scattering patterns on 512 bins to obtain the 1D I vs Q plots for each of the two dimensions. A logarithmic bin was applied to prevent overweighting of the fit to high Q.

2.6.3 Model fitting

SasView (version 5.0.2) was used to fit the scattering data to structural models

based on the scattering data. SAXS is implemented by using a scattering length density (SLD) of $14.025 \times 10^{-6} \text{ \AA}^{-2}$, which was used for 1ThNapFF and an SLD of $9.469 \times 10^{-6} \text{ \AA}^{-2}$, which was used for the solvent (water). For SANS, an SLD of $6.393 \times 10^{-6} \text{ \AA}^{-2}$ for 1ThNapFF and $2.377 \times 10^{-6} \text{ \AA}^{-2}$ for H₂O. We chose cylindrical models for 1ThNapFF that the molecules self-assemble into micelles that look like worms. The fitting was started by fitting the most simplistic cylinder models (with the fewest parameters) first and progressively moving up to more complex cylinder models. If more complex models were required, each model was chosen to confirm the final choice of the model that best fit the data and was then considered as whether what model should be used. To capture the high scattering intensity at low Q, in all the data sets, the cylinder model was combined with a power law model.

2.7 Hydrogel noodle formation, bridging and dry filament formation

The 1ThNapFF solutions were injected into a 50 mM CaCl₂ bath to prepare hydrogel noodles. The fluid was dispensed using a 2-20 μL pipette while dragging the pipette tip across the trigger medium to produce a linear noodle. A static injection generally leads to the production of noodles that have curved shapes, which can be difficult to bridge across gaps.

Tweezers were used to remove the noodles from the bath after they were injected for 5 - 10 seconds. They are picked up from one end, allowing the entire length of the noodles to span a gap. The gel noodles were wrapped around two parallel capillaries positioned on a support (generally a beaker or glass dish) and held in place using 'Blu-Tac' at a fixed distance. Afterward, they were dried overnight (covered with a large dish) or tested for mechanical strength.

The excess noodles at either end were wrapped to the capillary tube to secure the noodles in place during the tests of mechanical strength. In the absence of this, the noodle would slide off (instead of breaking) upon application of a mass, resulting in an inaccurate reading of the mass it could support. We tested the mechanical strength of the wet noodles by applying a 2 x 2 cm folded tin foil. We used a fixed 2 x 2 cm shape and added different layers to increase the mass. A single layer of 2 x 2 cm foil weighs 5 mg and a double layer of foil weighs 10 mg. For each NaCl equivalent, 7 noodles were prepared and loaded with weights until they broke. The noodle's maximum weight that it could support before it broke was recorded.

3. Results and discussion

3.1 Gel formation

We used the 'inverted vial' method to determine whether a pre-gel solution has formed a gel. The inverted vial method involves inverting the container containing the viscous immobile material after stimulating the formation of the immobile material and, after a period, if the system remains immobile, it can be tentatively concluded that a gel has formed.

Solutions of 1ThNapFF were prepared at a concentration of 10 mg/mL at a pH of 11.3 by deprotonation of the terminal carboxylic acid using sodium hydroxide. At this concentration, a viscous solution is formed (Figure 18). Similar solutions were prepared at the same concentration of 1ThNapFF and the same pH, but with the addition of different amounts of sodium chloride from 0 molar equivalent with respect to 1ThNapFF up to 10 molar equivalents. The addition of salt visibly affected the samples (Figure 18).

Based on the data from the inverted vial experiments, we determined that all other things being equal, no gels were formed in the samples with 0 molar equivalent (Figure 18a), 1 molar equivalent (Figure 18b), 2 molar equivalents (Figure 18c), 4 molar equivalents (Figure 18e), 5 molar equivalents (Figure 18f) and 7 molar equivalents (Figure 18h) of sodium chloride. In contrast, the samples with 3 molar equivalents (Figure 18d), 6 molar equivalents (Figure 18g), 8 molar equivalents (Figure 18i), 9 molar equivalents (Figure 18j) and 10 molar equivalents (Figure 18k) of sodium chloride formed gels. The samples that formed gels after the vial had been inverted for 1 min were not destroyed.

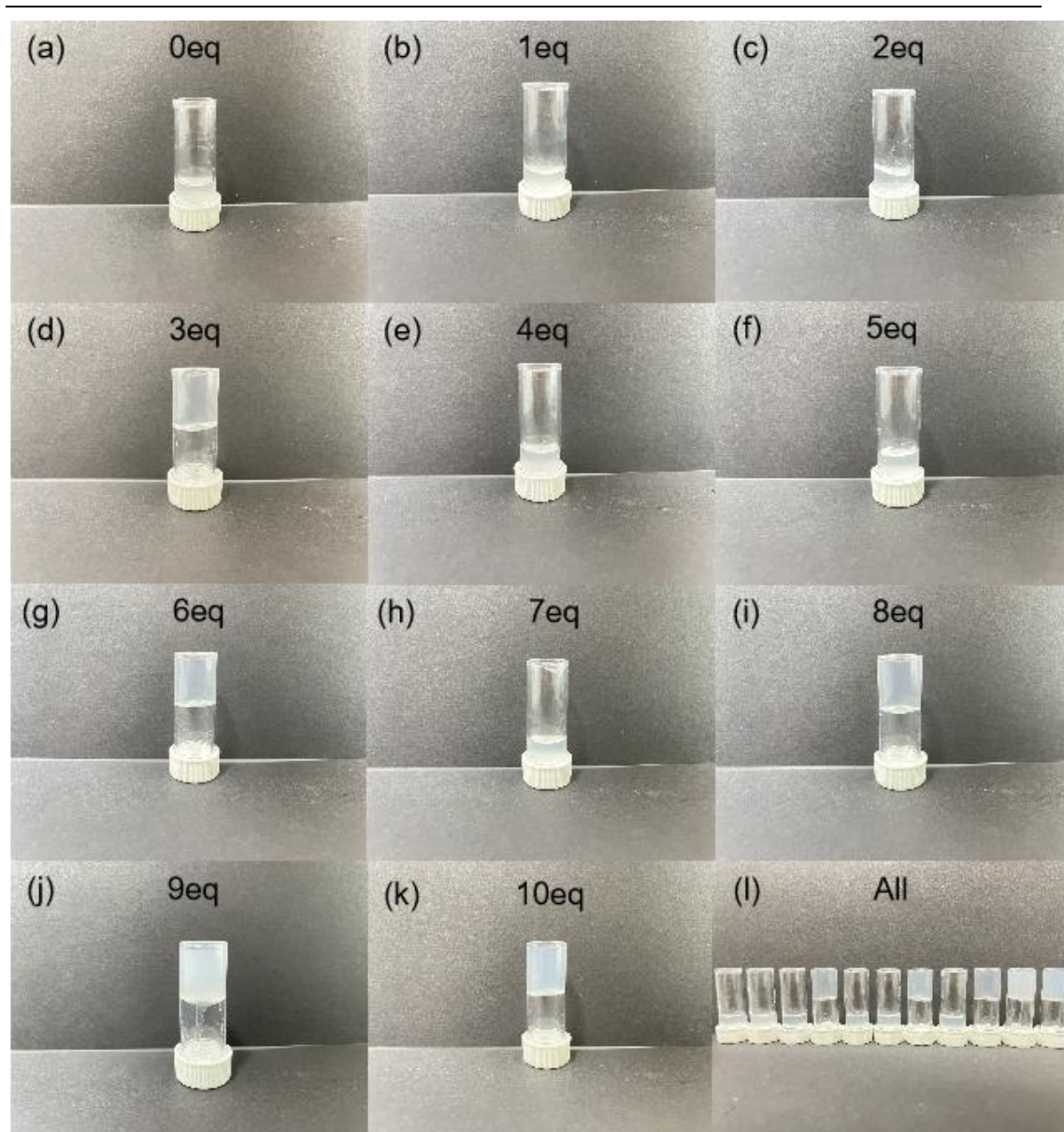


Figure 18. Performance of 1ThNapFF solution at a concentration of 10 mg/mL and pH 11.3 after addition of different 0 (a), 1 (b), 2 (c), 3 (d), 4 (e), 5 (f), 6 (g), 7 (h), 8 (i), 9 (j) and 10 (k) molar equivalents of NaCl in inverted vial. The molar equivalents of sodium chloride are compared with all samples placed together (l) in increasing order from left to right.

It is difficult to explain these visual observations and why 4, 5, and 7 eq. did not form gels. To try and understand this further, a number of other techniques were therefore used.

3.2 Rheological properties

Shear viscosity measurements were performed on 1ThNapFF solutions with 0 to 10 NaCl equivalents. Three replicates were performed for each NaCl eq. solution, resulting in a total of 33 measurements. The data show a trend with NaCl concentration where the viscosity at low shear rate (1 s^{-1}) increases gradually from 0 – 4 eq. NaCl. At 5 eq. NaCl, the viscosity then increases dramatically, reaching a peak

of 5 Pa.s at 6 eq. NaCl, with a viscosity approximately 10 times that of the 0 eq. solution. Moving to 7 eq. NaCl, the viscosity drops to 2 Pa.s and subsequently increases slightly from 8 to 10 eq. NaCl. From the experimental results, it is clear that 0 eq. has the lowest shear viscosity, but surprisingly the sample with the highest shear viscosity is 6 eq. (Figure 19).

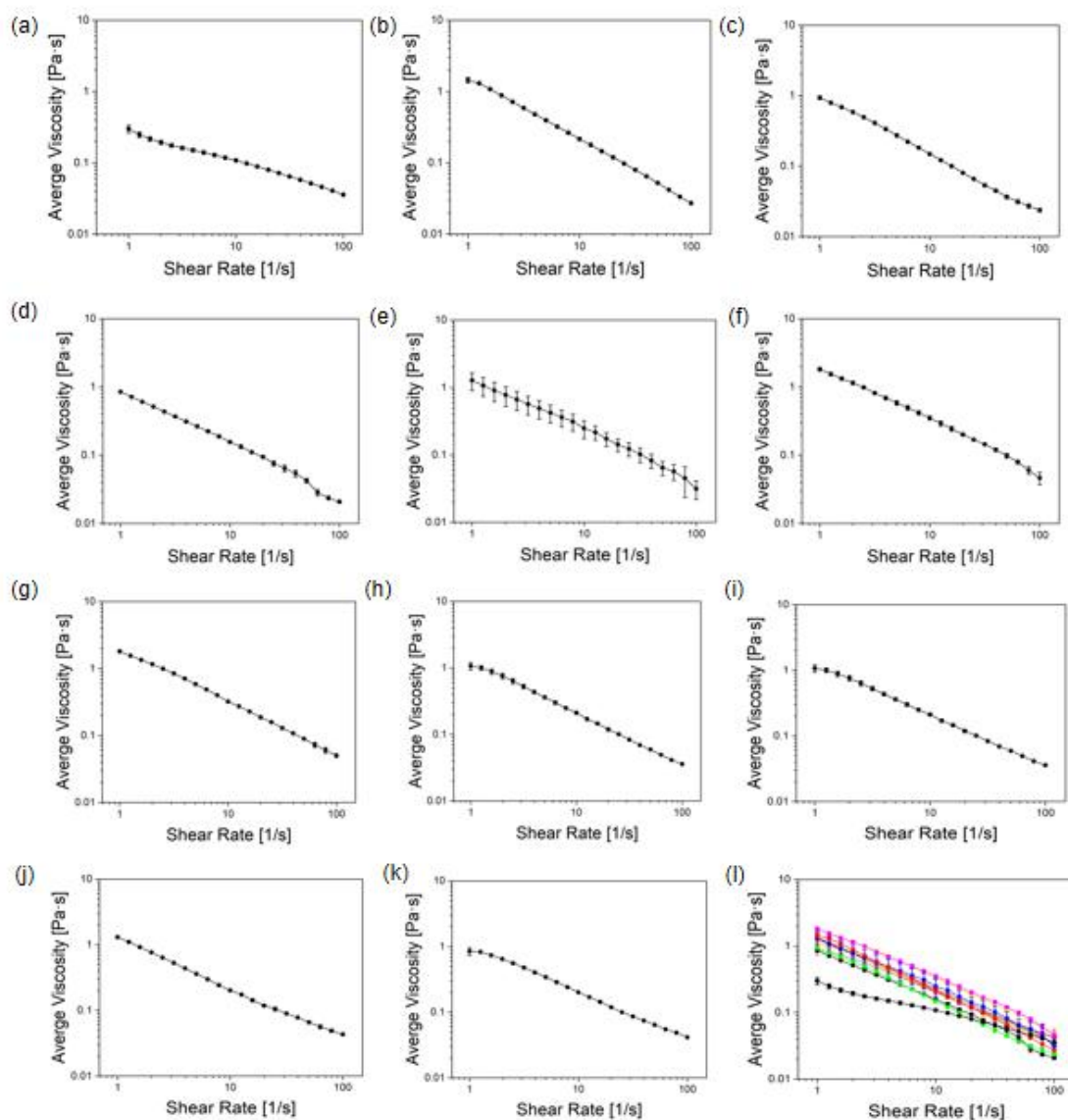


Figure 19. Shear viscosity data for 10 mg/mL 1ThNapFF solutions at pH 11.3 with different equivalents (a) 0 eq.; (b) 1 eq.; (c) 2 eq.; (d) 3 eq.; (e) 4 eq.; (f) 5 eq.; (g) 6 eq.; (h) 7 eq.; (i) 8 eq.; (j) 9 eq. and (k) 10 eq. NaCl. (l) compares all data.

Across the NaCl concentrations studied, all solutions have high viscosity compared to water alone and exhibit shear-thinning behaviour, which is indicative of WLM entanglement (Figure 20a).⁷⁰ Some solutions exhibit gel-like behavior as they can be inverted and do not appear to flow (Figure 18). As a means of investigating this effect more quantitatively, a small amplitude oscillatory shear rheology was applied (Figure

21). The data are best presented as NaCl concentration vs. $\tan \delta$ (Figure 20b), which is the ratio of the liquid-like (loss modulus G'') to solid-like (storage modulus G') characteristics. Based on the data obtained at 0 and 1 eq. NaCl, $\tan \delta > 1$, which indicates that liquid-like properties dominate and at 1 eq. NaCl $\tan \delta$ is approximately 1. In all other NaCl eq. $\tan \delta < 1$ means that solid-like features dominate. Nevertheless, for all samples, the value of $\tan \delta$ was not sufficient to define them as gels in the full sense of the word. The data are also plotted as a function of G' and G'' , where both values increase with increasing NaCl concentration up to 4 eq. NaCl and even if the NaCl eq. increases the value remain constant. There is a clear disconnect between the vial inversion and rheological data. We interpret this as a result of complex interactions of structural changes, persistent lengths and a tendency to form transient crosslinks through lateral associations. Subsequent observations under cross-polarization microscopy of solutions of different NaCl eq. showed the gradual appearance of crystals in the solution with the addition of NaCl eq. (Figure 22).

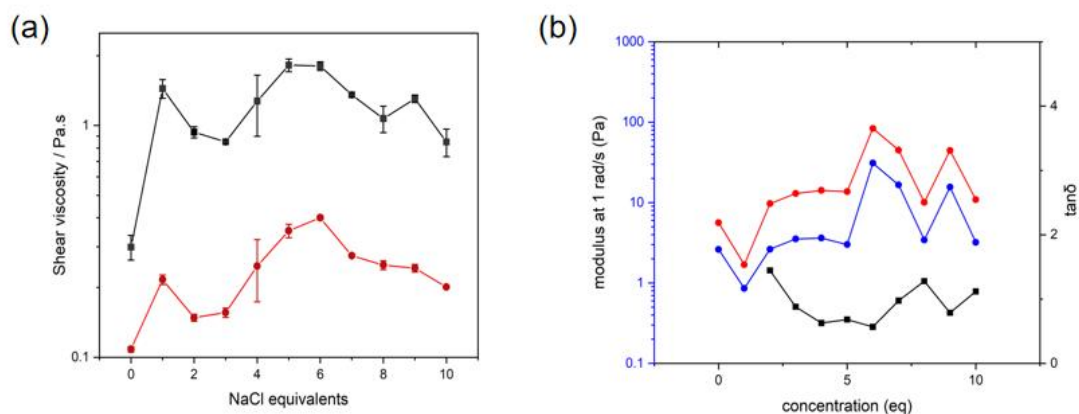


Figure 20. (a) plot of viscosity at 1 s^{-1} (black data) and 10 s^{-1} (red data) for the range of NaCl equivalents; (b) average $\tan \delta$ (black data, right axis) and average storage and loss moduli (red and blue data respectively, left axis) obtained from frequency sweeps of the 1ThNapFF solutions at 1% strain and 1 rad s^{-1} . The $\tan \delta$ data point for 0 and 1 eq. NaCl is > 2 and not displayed to better show trends in the other data.⁷¹ Reproduced from R. Huang, D. McDowall, H. Ng, L. Thomson, Y. K. Al-Hilaly, J. Douth, S. Burholt, L. Serpell, R. Poole and D. Adams, Chem. Commun., 2022, 58, 10388-10391, with permission from the Royal Society of Chemistry.

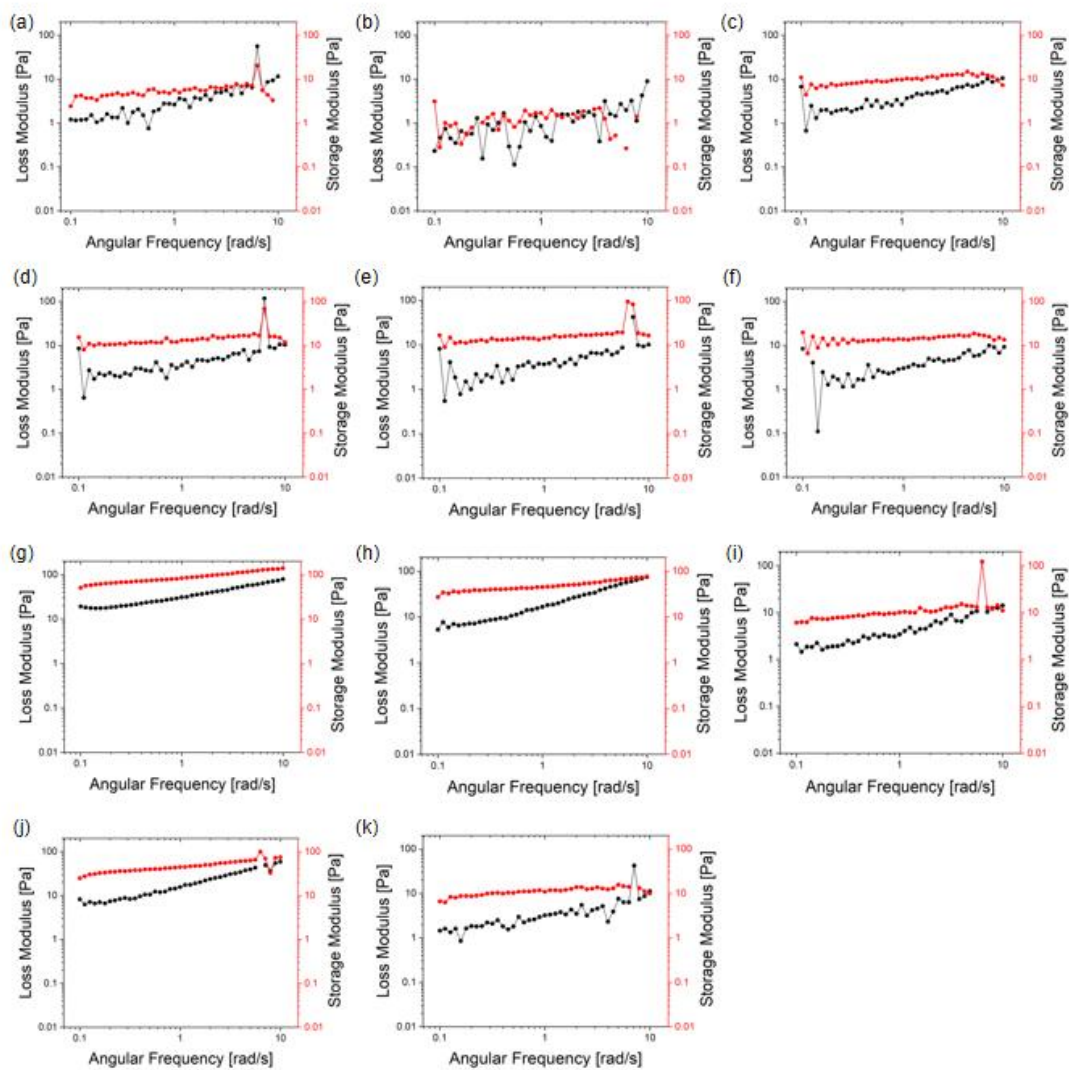


Figure 21. Oscillatory frequency sweeps data for (a) 0 eq.; (b) 1 eq.; (c) 2 eq.; (d) 3 eq.; (e) 4 eq.; (f) 5 eq.; (g) 6 eq.; (h) 7 eq.; (i) 8 eq.; (j) 9 eq. and (k) 10 eq. NaCl. Red is the storage modulus (G') and black is the loss modulus (G'').

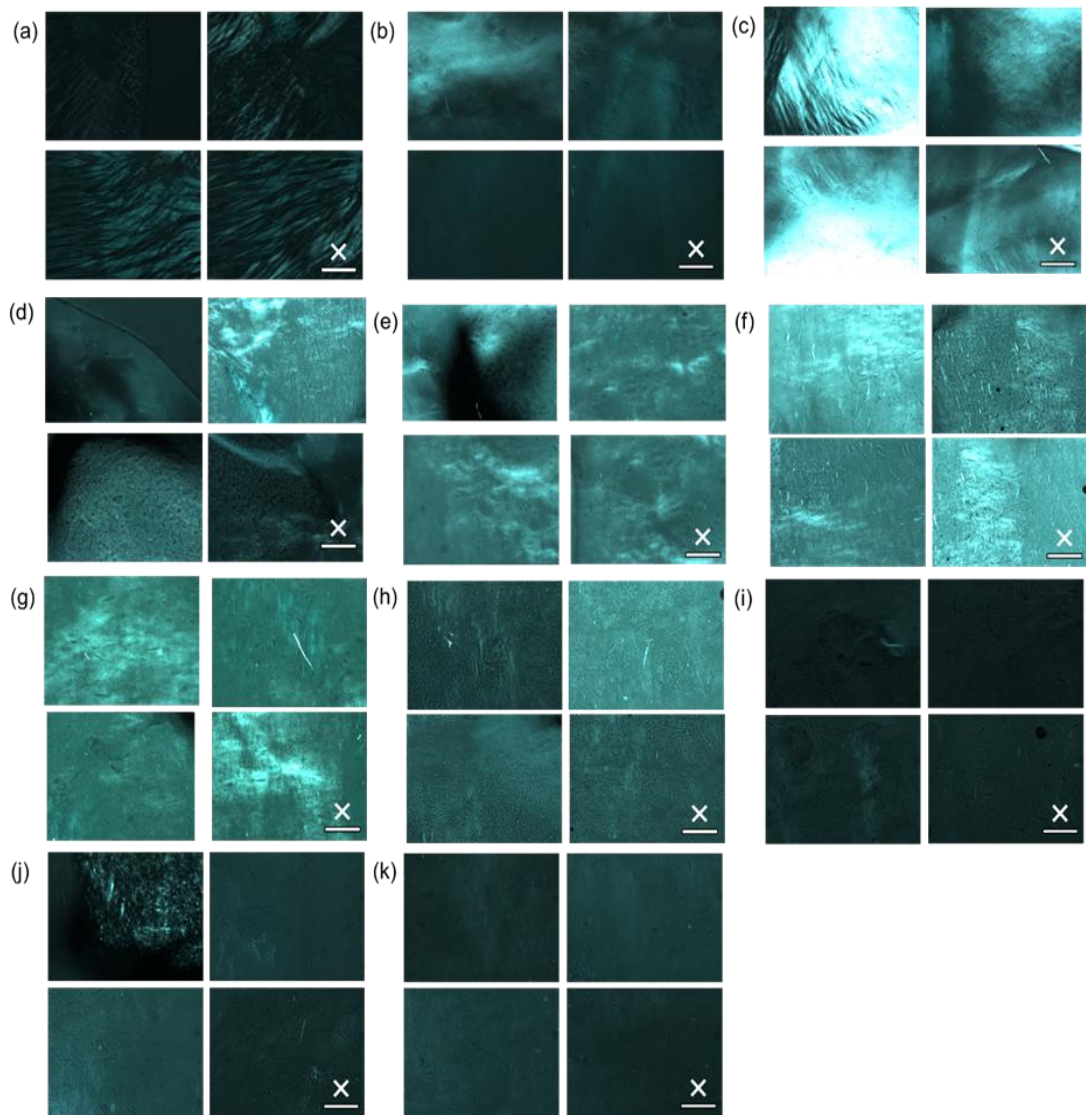


Figure 22. Cross-polarised microscopy images of 1ThNapFF solutions with different NaCl equivalents (a) 0 eq; (b) 1 eq; (c) 2 eq; (d) 3 eq; (e) 4 eq; (f) 5 eq; (g) 6 eq; (h) 7 eq; (i) 8 eq; (j) 9 eq and (k) 10 eq. Scale bar represents 0.5 mm and white crosses represent polariser directions.

3.3 Dripping-onto-substrate results

Extensional viscosity measurements were carried out using a dripping-onto-substrate (DoS) setup.⁶⁶ The technique involves the distribution of liquid droplets onto a surface, thereby forming an unstable liquid bridge. The subsequent thinning and rupture of the liquid bridge is determined by the material properties of the fluid.^{51, 66, 72} By video recording and analysing this process, various material properties can be obtained. DoS has been applied to a wide range of complex fluids and can be performed with relatively inexpensive equipment. During DoS measurements, polymer solutions and WLM solutions are typically characterized by their viscoelastic behaviour,⁷³ where at later stages of the thinning process a slender filament forms which undergoes uniaxial extensional flow. The thinning can be fitted with an exponential decay to obtain the extensional relaxation time (equation 4).

$$(4) \quad \frac{R}{R_0} = \left(\frac{G_E R_0}{2\sigma} \right)^{\frac{1}{3}} \exp \left(-\frac{t}{3\lambda_E} \right)$$

The G_E is the elastic modulus, λ_E the extensional relaxation time, R_0 radius of the dispensing needle, R filament radius and σ the surface tension.

An analysis was conducted using DoS on 1ThNapFF solutions with different NaCl equivalents. For each NaCl eq., three solutions were studied with three replicates performed for each solution, resulting in nine measurements (Figures 23, 24 and 25). Many of the liquid bridge thinning processes were multiple seconds long. For the exponential decay fitting, filament radius was only measured at later times in MatLab to save time and computing power. As such, the fits shown below, do not show filament radius for the entire process. Instead, from when a thin filament is forming. Data collection at maximum frame rate (240 fps) was not sufficient to fit the data accurately in some samples because filament breakage occurred very rapidly (Figure 26 0 eq., 6 eq. and 7 eq.).

As shown in Figure 26 (1 eq.), in other samples, the filament thinning also occurred on intermediate timescales, allowing the thinning process to be efficiently captured and fitted most accurately. Furthermore, some samples did not exceed a reasonable timescale (>2 min) and λ_E was not calculated (Figure 26 4 eq., 5 eq., 10 eq.); it does not necessarily mean that the λ_E is very high, but that the unstable liquid bridge has not yet formed and the dilution kinetics have not yet been inhibited.

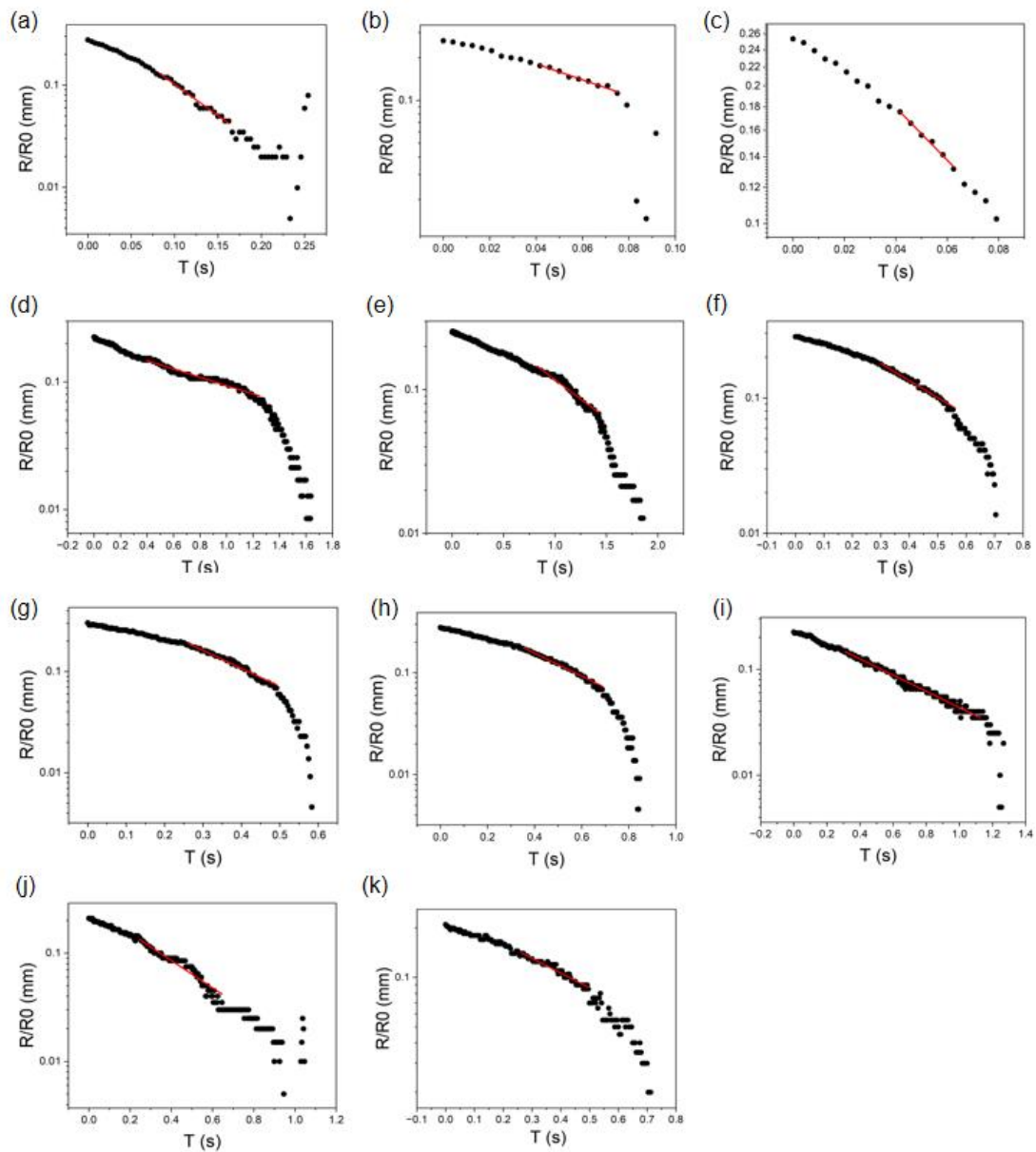


Figure 23. Exponential decay fits to aspect ratio 10 filaments for (a – c) 0 eq. NaCl; (d – k) 1 eq. NaCl.

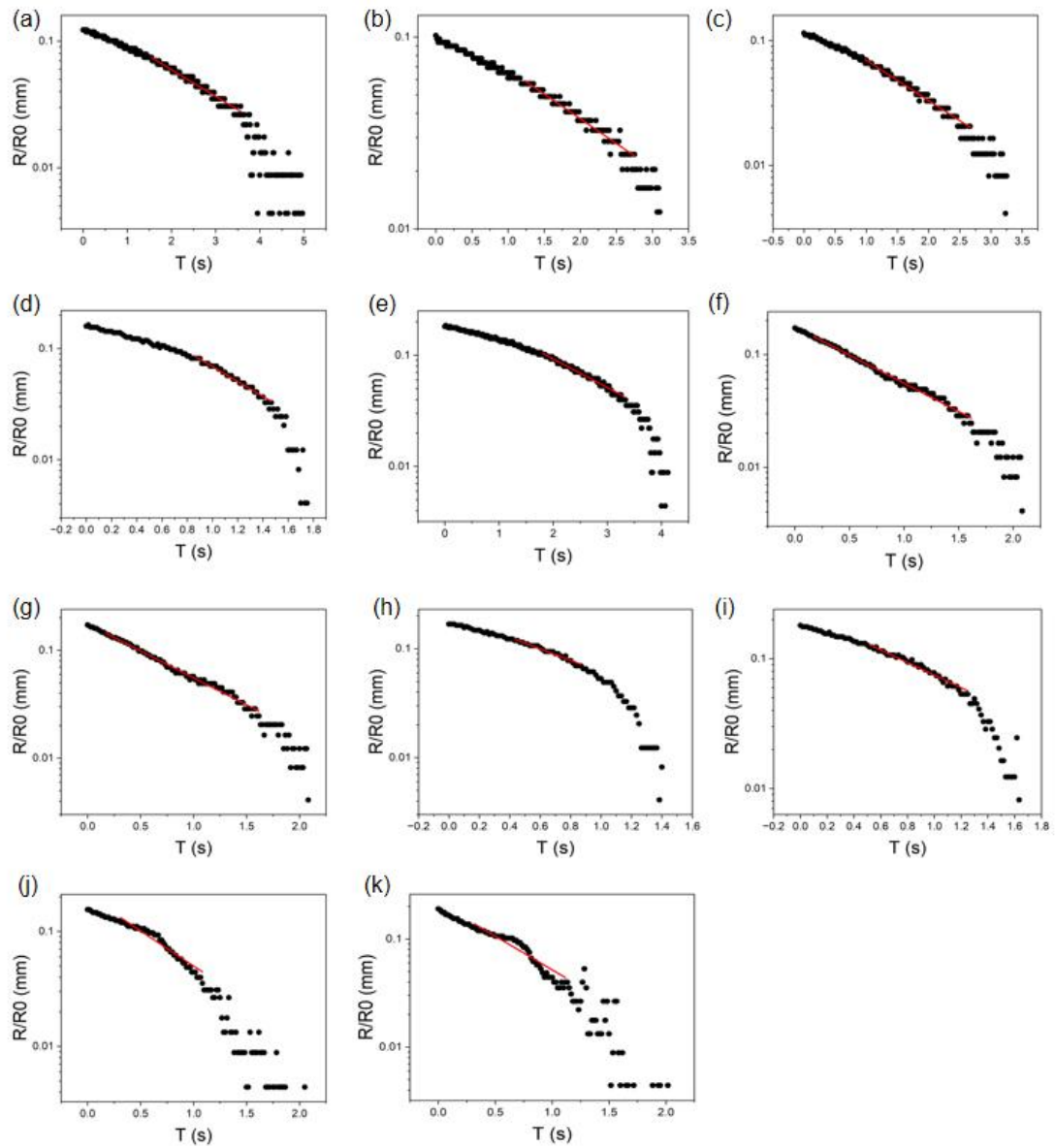


Figure 24. Exponential decay fits to aspect ratio 10 filaments for (a – d) 2 eq. NaCl; (e) 3 eq. NaCl; (f – h) 6 eq. NaCl and (i – k) 7 eq. NaCl.

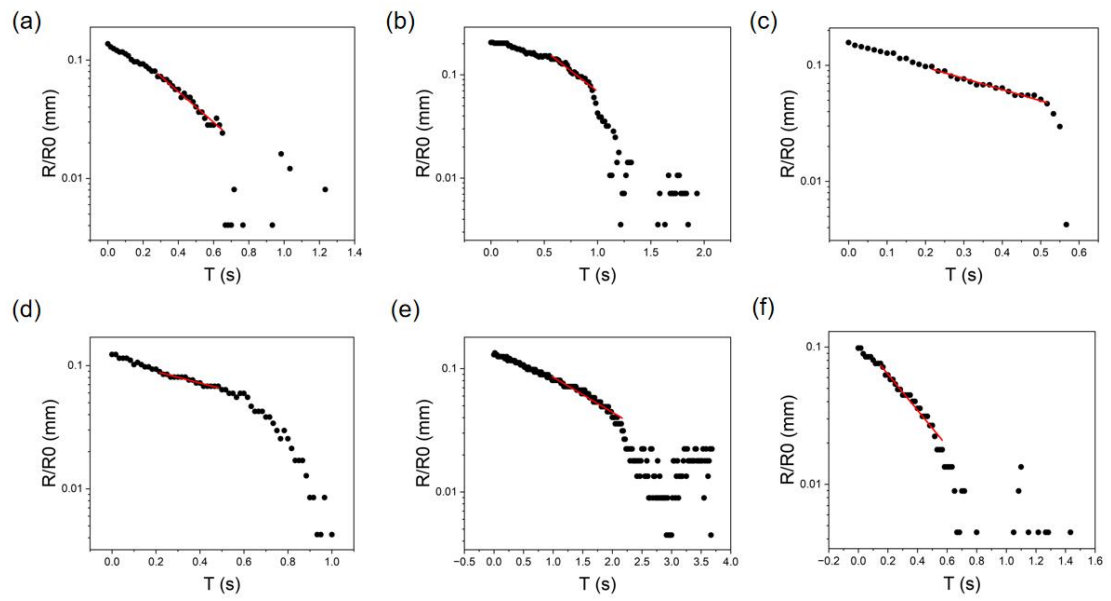


Figure 25. Exponential decay fits to aspect ratio 10 filaments for (a – b) 8 eq. NaCl and (c – f) 9 eq. NaCl.

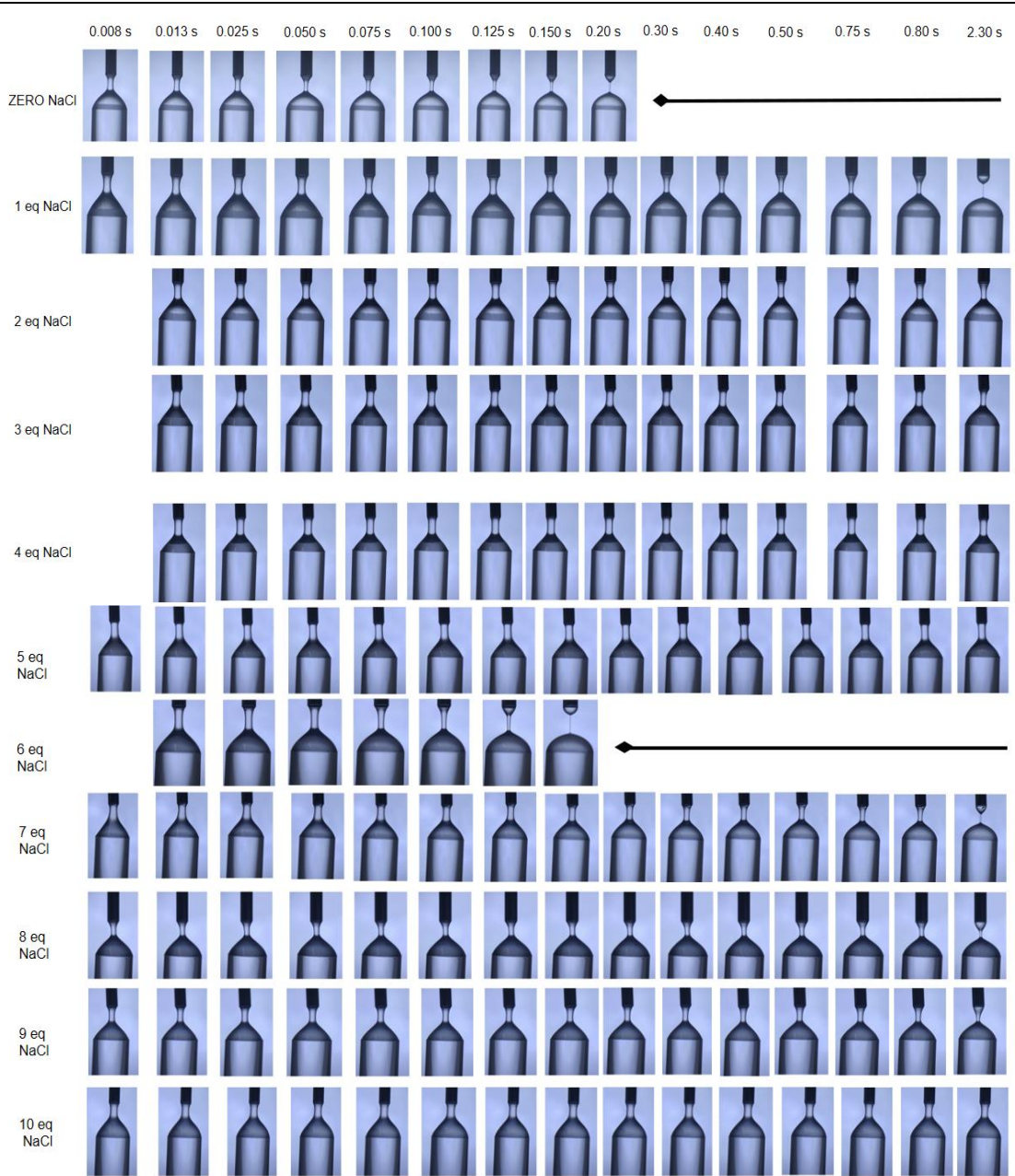


Figure 26. Summary of the DoS results for each NaCl equivalent include the images of a thinning process with fast thinning (0 eq, 6 eq and 7 eq. NaCl) and an intermediate thinning process with exponential decay (1 eq. NaCl) and no broken filament (4 eq, 5 eq and 10 eq. NaCl). Full details of the different behaviour seen can be found in Table 1.

Table 1. Summary of the DoS results for each NaCl equivalent. For each NaCl eq, 3 solutions were studied with 3 repeats each. Extensional relaxation times are given in seconds. Where the extensional relaxation time could not be measured, the filament either did not break or broke too rapidly to be fitted. *Excluded as an outlier on the basis of the very different value to the rest of the data.

	0eq	1eq	2eq	3eq	4eq	5eq	6eq	7eq	8eq	9eq	10eq
R1	0.096	*1.173	0.688	Did not break	Did not break	Did not break	0.277	0.154	Did not break	0.158	Did not break
R2	Too fast	0.445	Did not break	Did not break	Did not break	Did not break	0.274	0.237	Did not break	0.313	Did not break
R3	Too fast	0.267	0.214	Did not break	Did not break	Did not break	0.299	0.232	0.126	Could not be fitted	Did not break
R4	Too fast	0.116	0.56	0.563	Did not break	Did not break	Too fast	Too fast	Did not break	Could not be fitted	Did not break
R5	Too fast	0.08	Did not break	Did not break	Did not break	Did not break	Too fast	Too fast	Did not break	Did not break	Did not break
R6	Too fast	0.128	Did not break	Did not break	Did not break	Did not break	Too fast	Too fast	Did not break	Did not break	Did not break
R7	0.026	0.19	0.447	Did not break	Did not break	Did not break	Too fast	Too fast	Did not break	0.51	Did not break
R8	0.0297	0.115	Did not break	Did not break	Did not break	Did not break	Too fast	Too fast	Did not break	0.111	Did not break
R9	Too fast	0.161	Did not break	Did not break	Did not break	Did not break	Too fast	Too fast	0.182	Did not break	Did not break

According to all experimental data, the data at 0 eq. NaCl exhibited very fast breaks, where $\lambda_E < 0.1$ s or are too small to allow valid data to be obtained. At 1 eq. NaCl, exponential decay can be fitted to all samples and show an average relaxation time above 0 eq. NaCl. At 2 and 3 eq. NaCl, the filaments sometimes broke and the λ_E was measured, however, the majority did not break and the λ_E was not measured. Those that did break showed an increase in λ_E as the NaCl concentration increased for those who broke. At 4 and 5 eq. NaCl, the liquid bridge was not observed to break during the period examined. The behaviour begins to shift significantly with the further increase of NaCl eq. At 6 and 7 eq. NaCl, all filaments are broken, but either too fast to obtain valid data, or $\lambda_E \sim 0.2$ s. At 8, 9 and 10 eq. NaCl, while it is true that the samples show irreproducibility, there are clear trends across the NaCl series. An

increase or decrease in NaCl concentration modulates λ_E . There is a surprising result in 6 eq. NaCl has the highest shear viscosity at 1 s^{-1} (Figure 1), but the λ_E is relatively small.

To verify the reproducibility of the DoS technique, we recorded a 0.4 wt% polyacrylamide (PAM) and 70:30 (volume:volume) solution of glycerol using the DoS technique on the polymer solutions. For PAM solutions, five solutions were studied resulting in five measurements (Figure 27). The experimental data show that the reproducibility of the data is surprisingly consistent despite the comparison of the experimental results for five solutions of PAM solutions. According to the calculation, the average value of extensional relaxation times λ_E of 0.4 wt.% PAM solutions is 0.67, which is similar to the findings of Jelena et al.⁵¹ Finally, we conclude that the DoS technique is a good method for measuring extensional viscosity, and this technique can be competent for the measurement of extensional viscosity of many types of solutions.

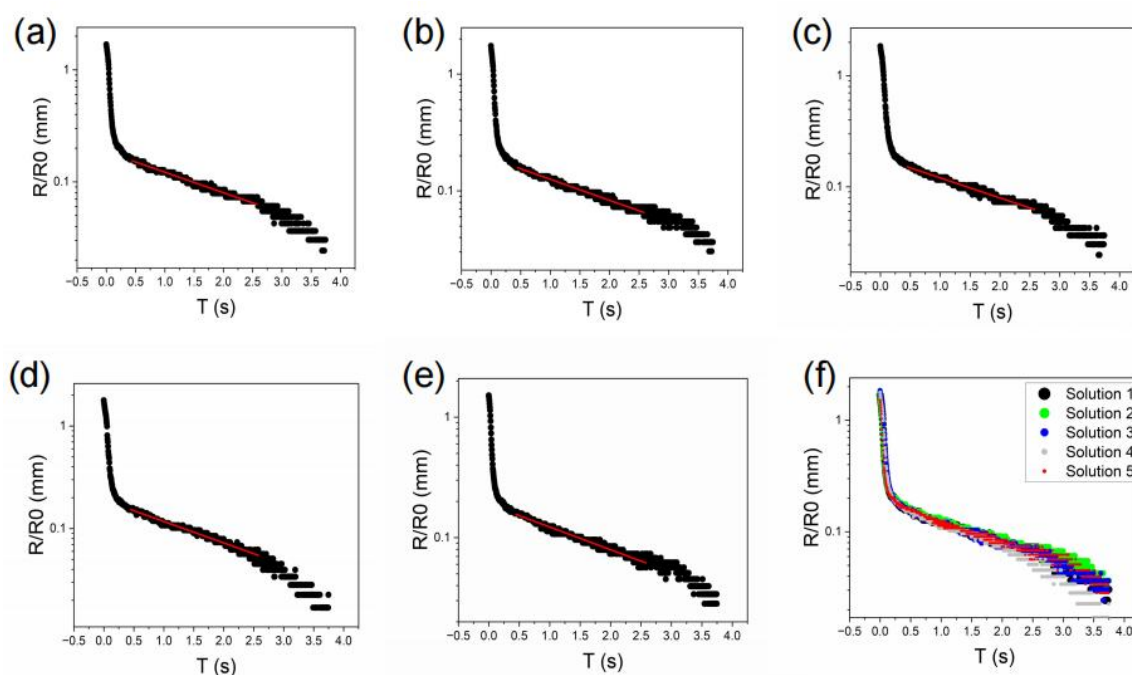


Figure 27. Exponential decay fits to aspect ratio 10 filaments for (a – e) 0.4 wt.% PAM solutions. Comparison of five solutions to show the high reproducibility (f).

3.4 Small angle scattering

To understand the key difference that how did the structure of the WLMs change with NaCl, we carried out small angle X-ray scattering (SAXS) and small angle neutron scattering (SANS) measurements, Figure 28. All small angle scattering measurements were carried out by Daniel McDowall or Lisa Thomson (University of Glasgow). The data were fitted by Daniel McDowall.

Due to the requirements for contrast, the SANS experiments were carried out in D_2O ,

whilst the SAXS experiments could be carried out in H₂O. The data show that the internal micelle structure is not affected by this change (Figure 29). Until 5 eq. of NaCl, similar long anisotropic structures form, and the SAXS data fits well with a power law and cylinder model. The radius across this range of NaCl is 2.4 ± 0.1 nm, with the length (assigned to the persistence length) around 50 nm. The data at 6 eq. of NaCl fit best to an elliptical cylinder model with a radius of 19 nm and an axis ratio of 2.7. At 7 eq. NaCl, the data are best fit to a cylinder combined with a power law. Here the fit now depicts 1D structures with a larger radius of 4.6 nm as compared with lower NaCl concentrations. At 8 eq., an adequate fit to the data could not be obtained with any model. At 9 and 10 eq. of NaCl, the data were best fit again to a cylinder model combined with a power law, also with a radius of 4.6 nm, and a similar persistence length of around 50 nm. All of this shows that a single model usually fits the data well. When multiple species are present, the data often cannot be fit to a single model or when significant polydispersity needs to be established. The SAXS data show that from low NaCl to high NaCl equivalents, the cylinder radius almost doubles. Confirmed by TEM, the structures formed at 6 eq. NaCl represent a point where there is a transition between structures rigid structures are formed with evidence for lateral association (Figure 28f). The requirement for an elliptical model, with a similar radius to those for 1 – 5 eq. points to lateral association of the WLM.⁷⁴ The SANS data at 0 eq. NaCl are best fit to a cylinder model at high Q, depicting 1.6 nm radius cylinders with a length of 27 nm. The fit was not extended to low Q owing to the presence of a structure factor peak at $Q = 0.019 \text{ \AA}^{-1}$. In the absence of salt, the WLM can be considered analogous to charged polyelectrolytes and this peak is attributed to the correlation length, ξ .⁷⁵ This is the length at which all charges are screened and corresponds to 32.4 nm here. At 1 eq. NaCl, the structure factor peak has disappeared, but the shape of the data is similar at high Q. These data were best fitted to a flexible cylinder model combined with a power law. The fit depicts similar structure to those at 0 eq. NaCl, but the loss of the structure factor peak suggests that surface charge has been screened by the NaCl. From the SANS data, the structures at 10 eq. NaCl fit best to a hollow cylinder combined with a power law model, implying that the core does not have sufficient contrast to be resolved by the SAXS measurements and the core of a hollow cylinder is stained. These data are confirmed by TEM (Figure 28g). The overall radius of the hollow tubes agrees with the cylinder radius found by SAXS.

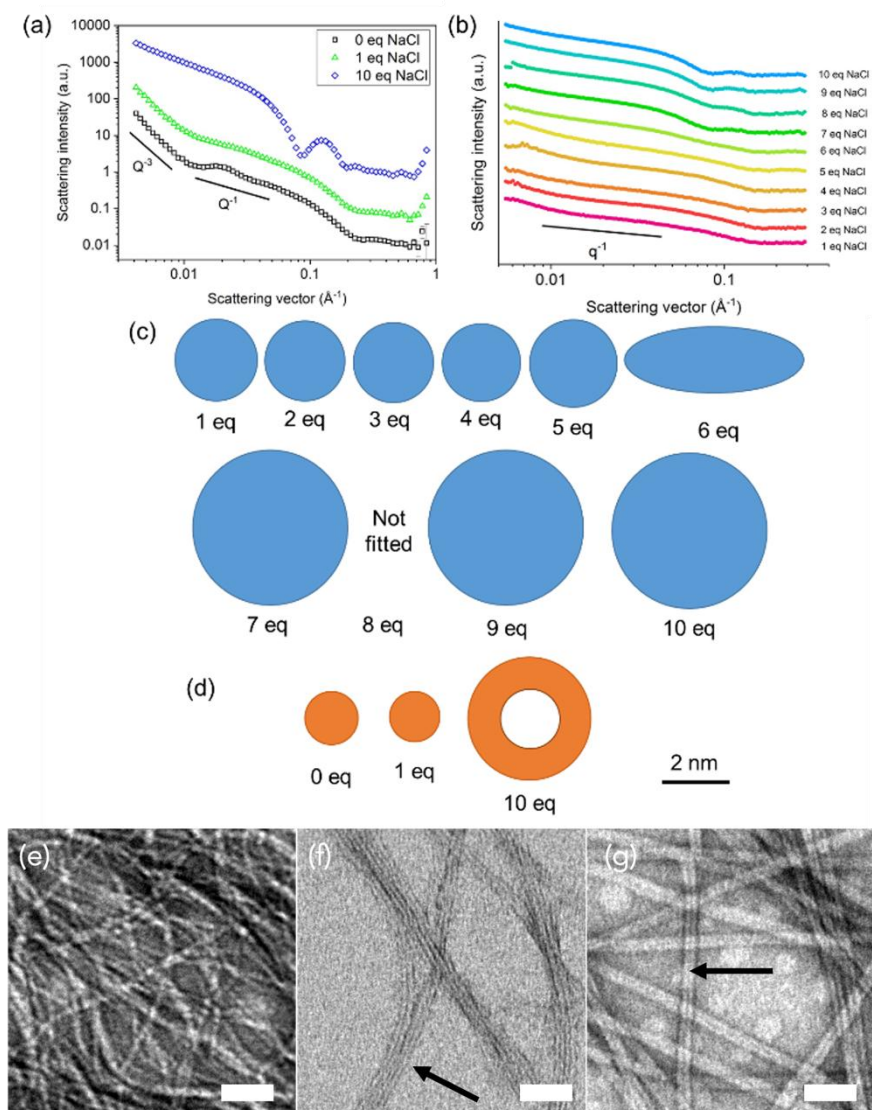


Figure 28. Scattering data (offset on y-axis for clarity) for solutions with different NaCl eq., (a) SANS data; (b) SAXS data; to scale cartoon of shape and cross-sectional areas of cylinders derived from fitting (c) SAXS and (d) SANS data. Scale bars = 2 nm; (e)–(g) TEM images for (e) 0 eq. NaCl; (f) 6 eq. NaCl; (g) 10 eq. NaCl. Scale bars = 40 nm. The arrow in (f) points to lateral association. The arrow in (g) points to the core of a hollow cylinder.⁷¹ Reproduced from ref. R. Huang, D. McDowall, H. Ng, L. Thomson, Y. K. Al-Hilaly, J. Douch, S. Burholt, L. Serpell, R. Poole and D. Adams, *Chem. Commun.*, 2022, 58, 10388-10391, with permission from the Royal Society of Chemistry.

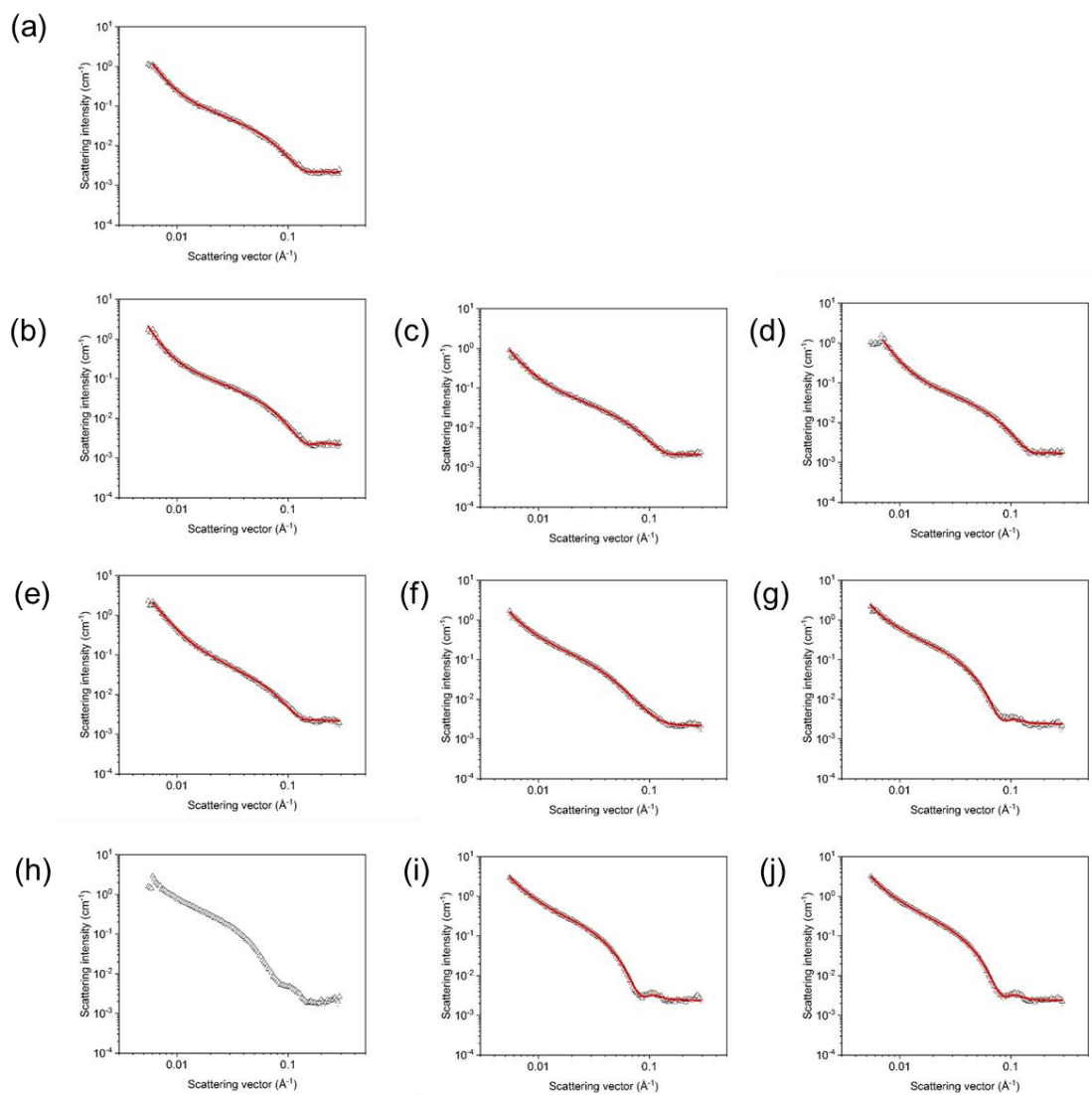


Figure 29. Small angle X-ray scattering data (hollow black triangles) and model fits (red lines; data for fits in Table 2) for (a) 1 eq NaCl; (b) 2 eq NaCl; (c) 3 eq NaCl; (d) 4 eq NaCl; (e) 5 eq NaCl; (f) 6 eq NaCl; (g) 7 eq NaCl; (h) 8 eq NaCl; (i) 9 eq NaCl and (j) 10 eq NaCl.

Table 2. Fitting parameters for SAXS data. In the model column cyl = cylinder, PL = power law and ell cyl = elliptical cylinder. 8 eq NaCl could not be fitted.

NaCl Eq	1	2	3	4	5	6	7	8	9	10
Model	Cyl + PL	Ell Cyl + PL	Cyl + PL	-	Cyl + PL	Cyl + PL				
Scale	0.00013	0.00018	0.00010	0.00015	0.00012	0.00014	0.00013	-	0.00014	0.00014
Scale error	2.1E-06	2.2E-06	2.3E-06	2.3E-06	2.0E-06	3.8E-06	6.3E-07	-	7.0E-07	7.1E-07
Background	0.0021	0.0022	0.0021	0.0017	0.0022	0.0022	0.0024	-	0.0024	0.0024
Background error	0.0001	0.0001	0.0001	0.0001	0.0001	0.0001	0.0001	-	0.0001	0.0001
Radius / Å	24.3	23.7	23.7	23.1	25.9	19.6	45.8	-	45.9	46.0
Radius error / Å	0.3	0.2	0.3	0.2	0.3	0.7	0.2	-	0.2	0.2
Axis ratio	-	-	-	-	-	2.7	-	-	-	-
Axis ratio error	-	-	-	-	-	0.1	-	-	-	-
Length / Å	556	370	504	407	192	5741	501	-	500	429
Length error / Å	90	24	91	51	13	3935	35	-	34	23
Power law scale	1.4E-10	3.9E-11	1.0E-09	2.9E-10	3.4E-08	1.7E-09	1.0E-09	-	5.6E-09	5.4E-09
Power law scale error	5.2E-11	1.4E-11	4.7E-10	7.1E-11	8.4E-09	1.0E-09	4.5E-10	-	1.8E-09	1.6E-09
Power law	4.4	4.7	3.9	4.4	3.5	3.9	4.1	-	3.8	3.8
Power law error	0.1	0.1	0.1	0.0	0.0	0.1	0.1	-	0.1	0.1
Reduced- χ^2	0.94	1.88	0.72	1.74	1.17	0.58	1.29	-	0.98	0.84

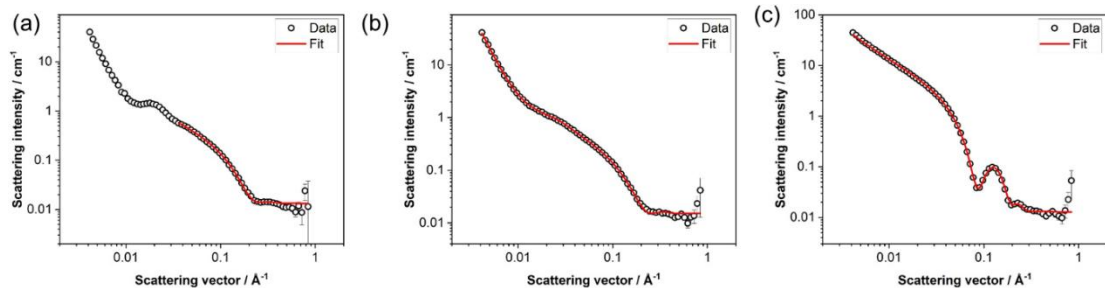


Figure 30. Small angle neutron scattering data (hollow black circles) with model fits (red lines) for (a) 0 eq NaCl; (b) 1 eq NaCl and (c) 10 eq NaCl.

A peak at $Q = 0.019 \text{ \AA}^{-1}$ was seen in the 0 eq NaCl data, which corresponds to 32.4 nm. A radius polydispersity of 0.15 was used to fit the hollow cylinder model. Without it, the fit line showed a more well-defined bump at $Q \sim 0.01 \text{ \AA}^{-1}$, thus missing the data. The loss of well-defined peaks in the data as compared to the fit can be due to either hollow cylinder polydispersity or instrument resolution.⁷⁶

Table 3. Fitting parameters for SANS data.

NaCl eq	0	1	10
Model	Cylinder	Flexible cylinder + power law	Hollow cylinder + power law
Scale	0.00584	0.006158	0.00763
Scale error	3.3E-05	3.6E-05	5.9E-05
Background	0.013	0.015	0.013
Background error	0.000	0.006	0.008
Radius / Å	15.7	14.9	17.6
Radius error / Å	0.1	0.1	0.1
Length / Å	274	182	4311
Length error / Å	29	3	59
Kuhn length / Å	-	120	-
Kuhn length error / Å	-	2	-
Thickness / Å	-	-	18.8
Thickness error / Å	-	-	0.1
Power law scale	-	7.5E-08	2.5E-05
Power law scale error	-	1.4E-08	3.5E-06
Power law	-	3.7	2.4
Power law error	-	0.0	0.0
Reduced- χ^2	3.2	2.0	6.9
Comment	Fit excludes low Q where structure factor peak is	-	Polydispersity radius 0.15

3.5 Microscopy data

According to the experimental data of small angle scattering, different results are shown for each sample. To further explore and verify the characteristics of each sample, we then investigated the formation of hydrogel noodles using the 1ThNapFF solutions at different NaCl eq. We prepared 1ThNapFF gel noodles by mimicking Zhang's experiment in which 20 μ L of a precursor solution was injected through a 0-

20 μL pipette into a bath containing a calcium chloride solution.⁵² Cross-linking of this solution containing WLMs occurs through chelation of calcium ions by the carboxylates on 1ThNapFF.⁵³ Gel noodles were readily formed at all NaCl equivalents (Figure 31). Across the range of samples, very limited birefringence is seen in cross polariser optical microscopy (CPOM), suggesting that the structures within the noodles are unaligned. Interestingly, the noodle structures formed solutions at 0 – 5 eq. NaCl have a rough surface whereas the noodles formed from solutions at 6 – 10 eq. NaCl exhibit much smoother surfaces.

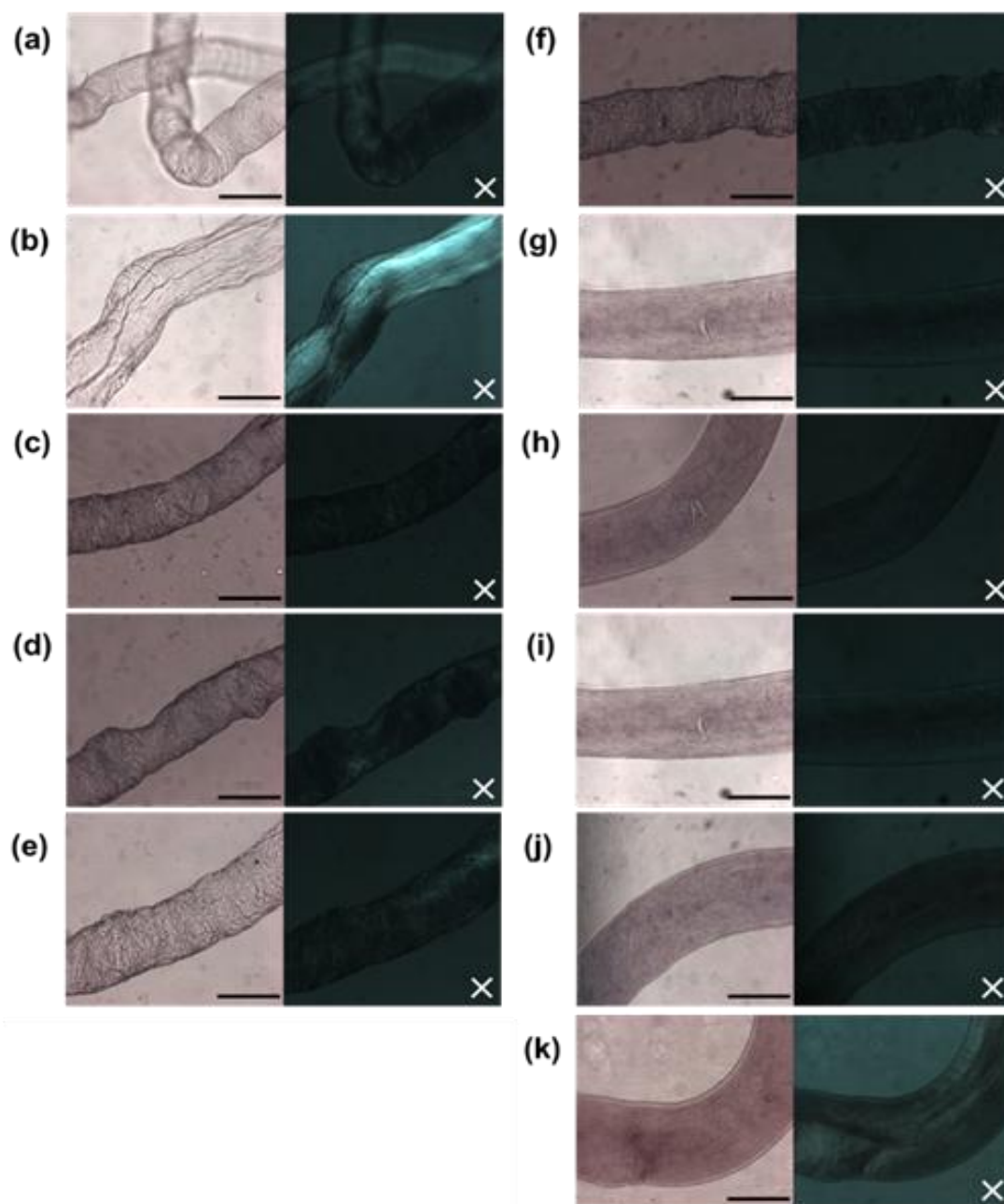


Figure 31. 5X microscope images of hydrogel noodles formed in a 50 mM CaCl_2 trigger bath using 10 mg/mL 1ThNapFF solutions with (a) 0 eq.; (b) 1 eq.; (c) 2 eq.; (d) 3 eq.; (e) 4 eq.; (f) 5 eq.; (g) 6 eq.; (h) 7 eq.; (i) 8 eq.; (j) 9 eq. and (k) 10 eq. NaCl. Noodles are imaged wet in a pool of trigger medium. For each sample left hand images are under normal light and right hand images under cross polarised light. The scale bars represent 0.4 mm and the white crosses denote the

polariser directions.

Using the above-mentioned technique of Temperta et al., very slim drawn gel noodles can also be formed (Figure 9).⁵⁴ This method involves pulling the gel noodles away from the tip of the pipette used to dispense the fluid with tweezers. As the gel noodles are formed, the process creates a stretching deformation in the fluid, resulting in very thin filaments. In addition, all concentrations of gel noodles were dried overnight and observed with a 20x microscope. For 0 - 5 eq. NaCl, the resulting gel filaments exhibit birefringence in the CPOM images and more clearly under polarized light (Figures 32a to 32f), indicating nanostructural alignment. At 6 - 10 eq. NaCl, the gel filaments are dark in the cross-polarised images (Figures 32g to 32k), indicating unaligned nanostructures. Strangely, 1-6 eq. NaCl of gel noodles glowed with a purple colour under the polarized light of a 20x microscope when the gel noodles dried overnight. And as the concentration increases, the purple gradually fades, and the samples after 6 eq. NaCl lose purple, and the 7-10 eq. NaCl emit more obvious light under polarized light. All this suggests that the different interactions between the WLM and different structures brought about by the different amounts of NaCl change the phases present.

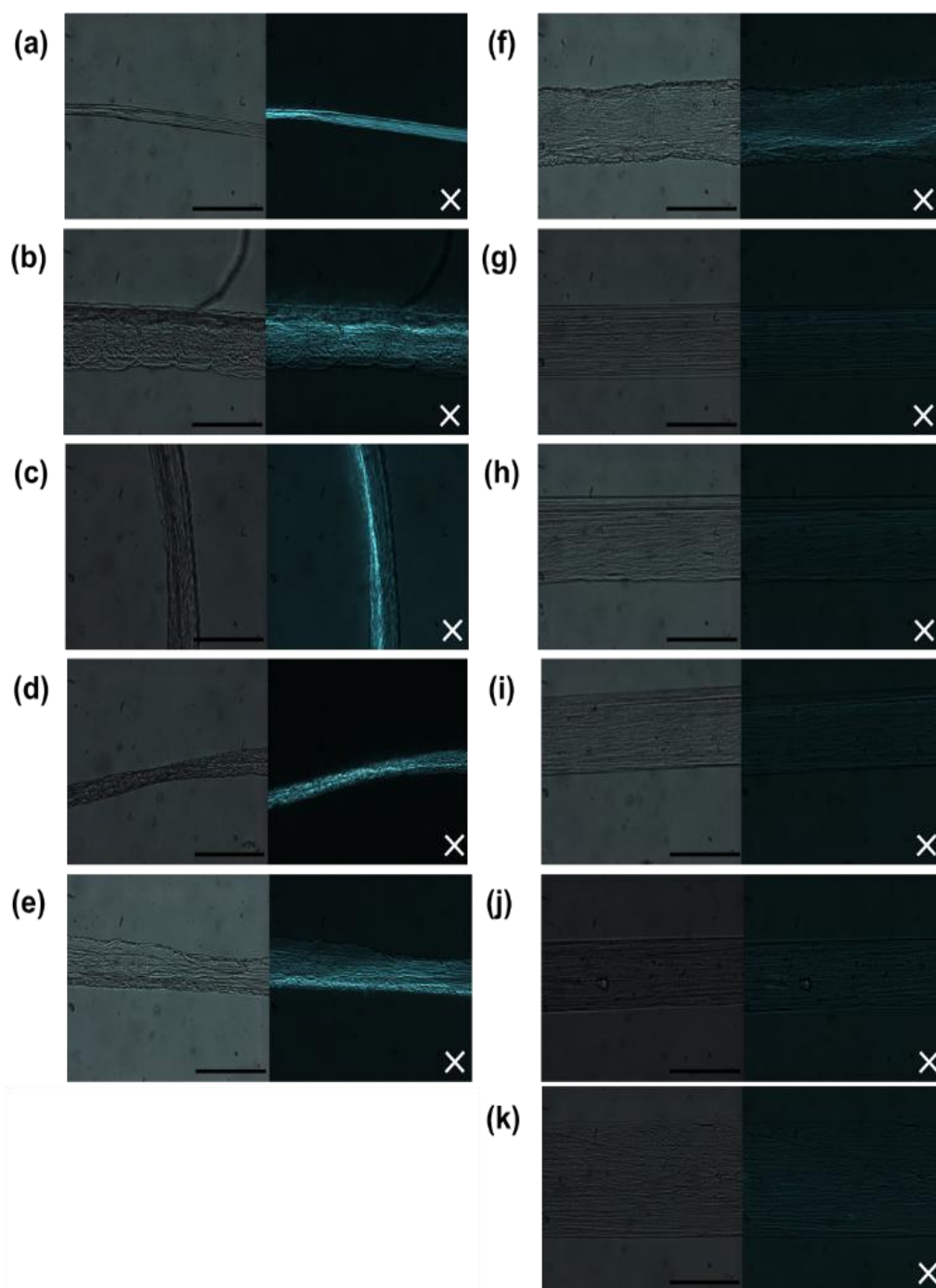


Figure 32. 20X microscope images of tweezer-drawn hydrogel noodles formed in a 50 mM CaCl_2 trigger bath using 10 mg/mL 1ThNapFF solutions with (a) 0 eq.; (b) 1 eq.; (c) 2 eq.; (d) 3 eq.; (e) 4 eq.; (f) 5 eq.; (g) 6 eq.; (h) 7 eq.; (i) 8 eq.; (j) 9 eq. and (k) 10 eq. NaCl. Noodles are imaged wet in a pool of trigger medium. For each sample left hand images are under normal light and right hand images under cross polarised light. The scale bars represent 0.2 mm and the white crosses denote the polariser directions.

Summing up all the above data, for the different solutions of 1ThNapFF, in 0 eq. NaCl samples, charged WLM have significant electrostatic repulsion. However, in 1-5 eq. NaCl the structure of the WLM remains unchanged, but the surface charge is shielded

by the presence of NaCl, allowing the micelles to pack closer together. Significant lateral association of the cylindrical WLMs occurs at 6 eq. NaCl, captured in the fit to the SAXS data as a need for ellipticity (Figure 33).⁷⁴ Between 7 and 10 eq. of NaCl, the self-assembled structure becomes a hollow cylinder with a larger diameter. As a result, noodles with different properties are formed from each of these solutions.

We imaged the noodles further by SEM (Figure 34), but highlight that there may be the influence of possible drying effects on the experimental data. It was found that the surface of the gel noodles of 1 eq NaCl made with tweezers was full of pores (Figure 34f). In many of the SEM images small crystals can be seen deposited on the surface of the structures (Figure 34a, 34c, 34g and 34h). Unsurprisingly, energy disperse X-ray (EDX) analysis showed these crystals to comprise predominantly of Ca, Cl and Na atoms (Figure 34i).

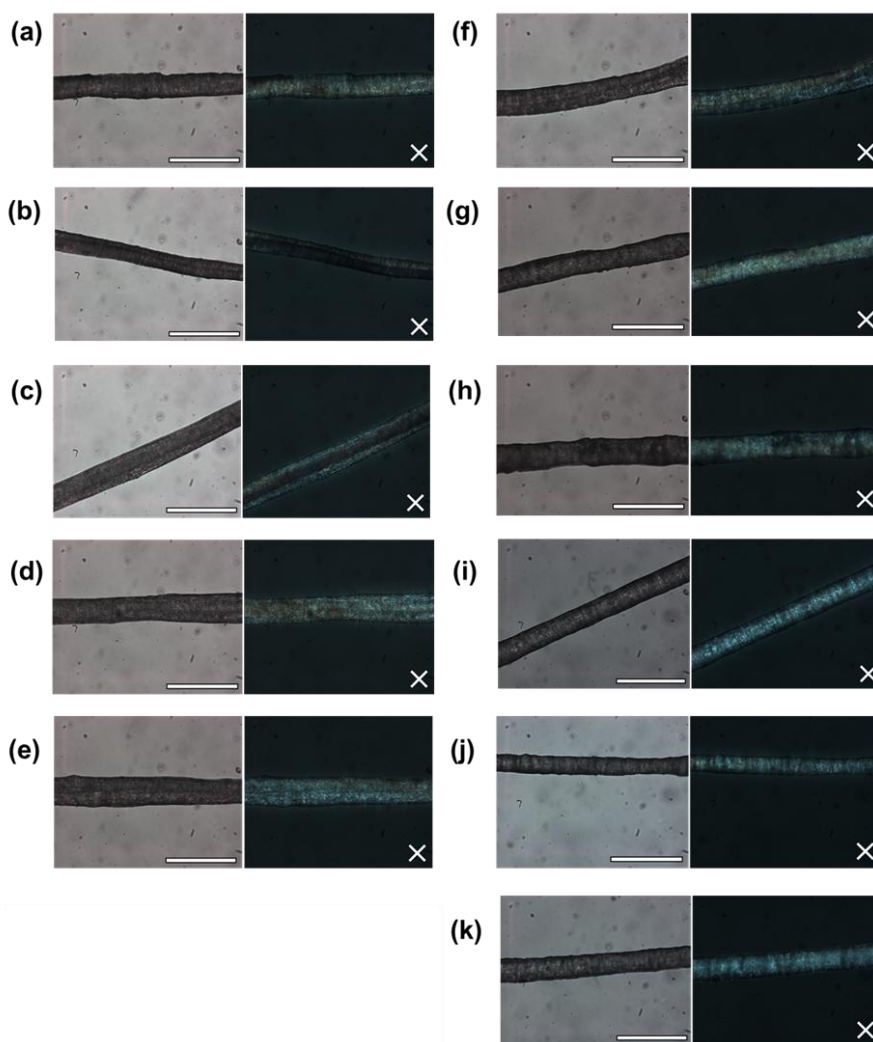


Figure 33. 20X magnification microscope images of static formed gel noodles air dried across a bridge for (a) 0 eq.; (b) 1 eq.; (c) 2 eq.; (d) 3 eq.; (e) 4 eq.; (f) 5 eq.; (g) 6 eq.; (h) 7 eq.; (i) 8 eq.; (j) 9 eq. and (k) 10 eq. NaCl. For each sample left hand images are under normal light and right-hand images under cross polarised light. Scale bars represent 0.2 mm and white cross indicates polariser direction.

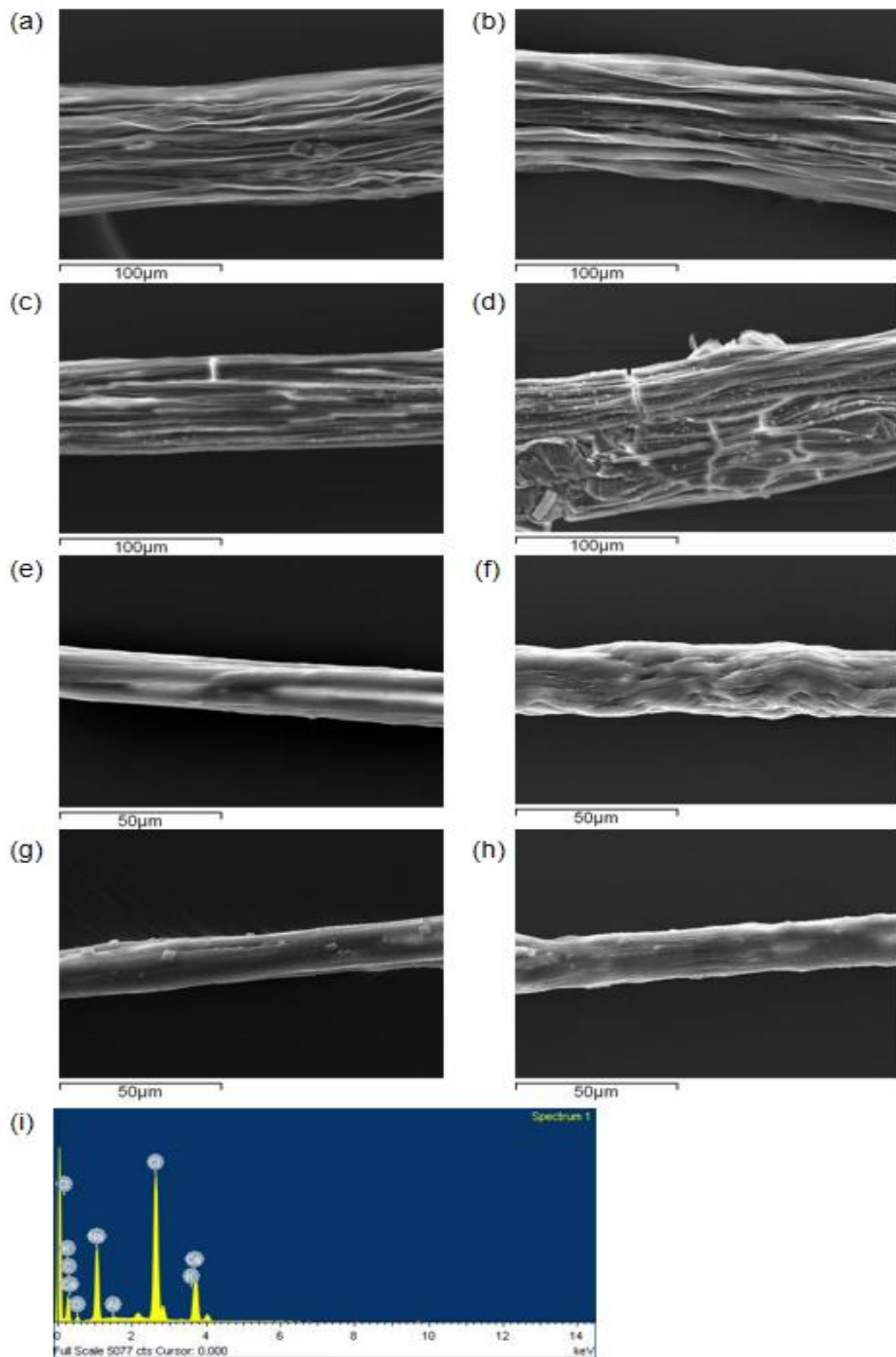


Figure 34. SEM images of static formed gel noodles air dried across a bridge for (a) 0 eq; (b) 1 eq; (c) 6 eq; (d) 10 eq NaCl. And the SEM images of drawn gel noodles air dried across a bridge for (e) 0 eq; (f) 1 eq; (g) 6 eq; (h) 10 eq NaCl. (i) Energy disperse X-ray (EDX) analysis of the noodle shown in (b).

The gel noodles are mechanically robust enough to be lifted out of solution with tweezers and bridged across a 3 cm wide gap. If left overnight, the noodles dry out, resulting in thin filaments. The dried filaments were imaged using both CPOM and scanning electron microscopy (SEM) (Figure 32 and 33). The drying process results in a thinning of the filaments to approximately 0.1 mm in diameter. In the CPOM images, the filament exhibit birefringence and in the SEM images the filaments appear to be comprised of bundles of fibres that are uniaxially aligned. The alignment appears to be a result of the drying process because the wet hydrogel noodles do not show birefringence.

3.6 Bridge load test

We discovered an interesting phenomenon when making gel noodles. Some gel noodles have strong mechanical properties, while others are very easy to break. We then adopted bridge loading experiments to explore the properties of the mechanical strength of wet gel noodles with different eq. NaCl (Figure 35a). When the gel noodles were formed in the calcium chloride solution bath, they were lifted with tweezers and placed on two capillary glass bridges at a distance of 3 cm apart, and the excess gel noodles were wrapped around the glass capillaries for fixing. The gel noodles with specific eq. NaCl have good flexibility. We then loaded each sheet of 2 × 2 cm of aluminium foil with a weight of 5 mg onto the bridge. The breaking strength of the gel noodles was tested by folding multiple times to achieve different weights of aluminium foil. From 0 to 5 eq. NaCl, gel noodle bridges can hold masses of 10-15 mg (Figure 35b). Surprisingly, the noodles at 6 eq. NaCl were the weakest and could only carry a weight of 5mg. From 7 to 10 eq. NaCl, the load-carrying capacity of the noodles rose rapidly and reached a maximum of 70 mg at 10 eq. NaCl. The structural changes in the WLM described above resulted in differences in the mechanical properties of the resulting gel noodles. The gel noodles that can withstand the greatest load are those made of hollow cylindrical WLM.

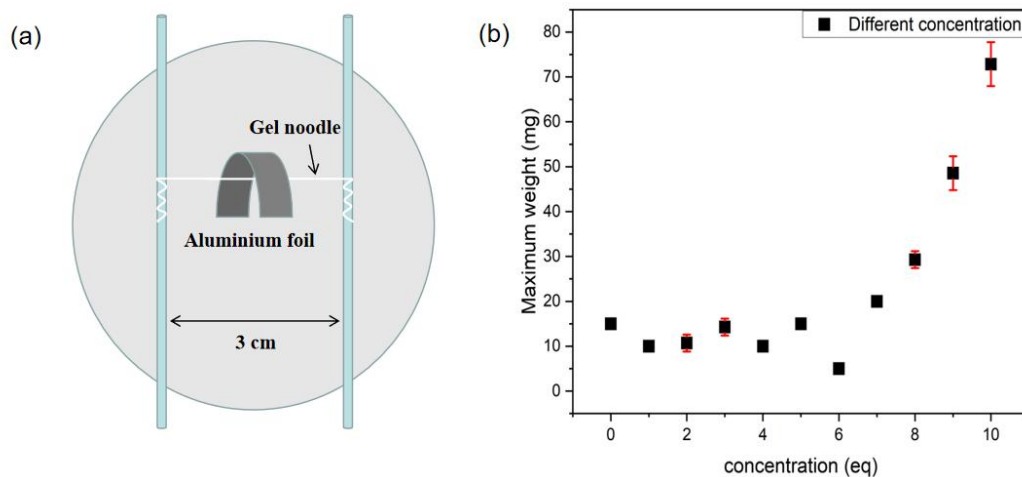


Figure 35. (a) Example photograph of gel noodle bridging experiments. (b) NaCl equivalents in pregel solution versus loading. The data points show the maximum load that the gel noodle bridge can support. Error bars represent the standard deviation of 7 replicate measurements, with small errors in most cases.

4. Conclusions

The functionalised dipeptide 1ThNapFF forms WLMs in high pH water, resulting in a viscous shear-thinning solution. Its behaviour is similar to that of a surfactant in that the structure of the worm-like micelles and their interactions change significantly by varying the NaCl concentration. The WLM structure remains unchanged until 6 eq. NaCl, where small-angle scattering indicates that lateral association of cylindrical fibres is occurring. Large hollow cylinders then form as the NaCl increases further. This has a profound effect on both the shear and tensile viscosity of the fluid. The shear viscosity reaches a maximum at 6 eq. NaCl, while the same fluids have some of the smallest tensile relaxation times. This has a profound effect on both the shear and tensile viscosity of the fluid. The shear viscosity reaches a maximum at 6 eq. NaCl, while the same fluids have some of the smallest tensile relaxation times. The charge effect produced by the increase of NaCl concentration changes the order of the internal structure of the sample and finally forms gel noodles with high mechanical strength (Figure 36). From these different fluids, gel noodles with different mechanical strengths and arrangements can be prepared.

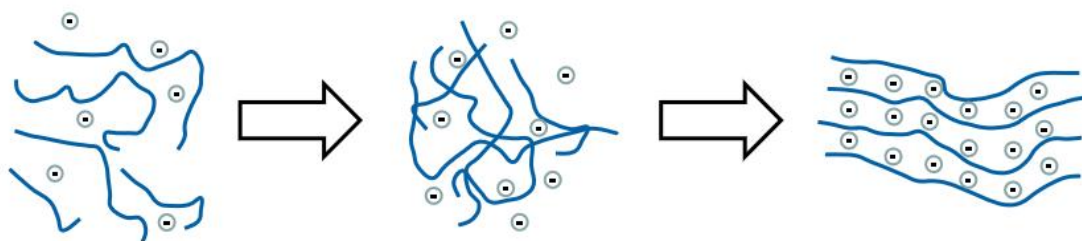


Figure 36. Schematic diagram of the change of the internal structure of the gel with the concentration of NaCl which leads to an increased screening in charge and so the potential to pack WLM more closely.

5. References

1. E. Busseron, Y. Ruff, E. Moulin and N. Giuseppone, *Nanoscale*, 2013, **5**, 7098-7140.
2. J. W. Steed and P. A. Gale, *Supramolecular chemistry: from molecules to nanomaterials*, Wiley, 2012.
3. Z. Wang, H. Wang, W. Zheng, J. Zhang, Q. Zhao, S. Wang, Z. Yang and D. Kong, *Chemical Communications*, 2011, **47**, 8901-8903.
4. R. G. Weiss, *Journal of the American Chemical Society*, 2014, **136**, 7519-7530.
5. C. D. Jones and J. W. Steed, *Chemical Society Reviews*, 2016, **45**, 6546-6596.
6. N. M. Sangeetha and U. Maitra, *Chemical Society Reviews*, 2005, **34**, 821-836.
7. P. Liang, C.-J. Liu, R.-X. Zhuo and S.-X. Cheng, *Journal of Materials Chemistry B*, 2013, **1**, 4243-4250.
8. F. M. Menger and K. L. Caran, *Journal of the American Chemical Society*, 2000, **122**, 11679-11691.
9. E. F. Banwell, E. S. Abelardo, D. J. Adams, M. A. Birchall, A. Corrigan, A. M. Donald, M. Kirkland, L. C. Serpell, M. F. Butler and D. N. Woolfson, *Nature Materials*, 2009, **8**, 596-600.
10. L. Chen, J. Raeburn, S. Sutton, D. G. Spiller, J. Williams, J. S. Sharp, P. C. Griffiths, R. K. Heenan, S. M. King and A. Paul, *Soft Matter*, 2011, **7**, 9721-9727.
11. S. Díaz-Oltra, C. Berdugo, J. F. Miravet and B. Escuder, *New Journal of Chemistry*, 2015, **39**, 3785-3791.
12. S. J. Wezenberg, C. M. Croisetu, M. C. Stuart and B. L. Feringa, *Chemical science*, 2016, **7**, 4341-4346.
13. W. Liyanage, W. W. Brennessel and B. L. Nilsson, *Langmuir*, 2015, **31**, 9933-9942.
14. Y. Xu, C. Kang, Y. Chen, Z. Bian, X. Qiu, L. Gao and Q. Meng, *Chemistry—A European Journal*, 2012, **18**, 16955-16961.
15. D. J. Adams, K. Morris, L. Chen, L. C. Serpell, J. Bacsá and G. M. Day, *Soft Matter*, 2010, **6**, 4144-4156.
16. E. C. Barker, A. D. Martin, C. J. Garvey, C. Y. Goh, F. Jones, M. Mocerino, B. W. Skelton, M. I. Ogden and T. Becker, *Soft Matter*, 2017, **13**, 1006-1011.
17. M. De Loos, B. L. Feringa and J. H. van Esch, *European Journal of Organic Chemistry*, 2005, **2005**, 3615-3631.
18. K. McAulay, B. Dietrich, H. Su, M. T. Scott, S. Rogers, Y. K. Al-Hilaly, H. Cui, L. C. Serpell, A. M. Seddon and E. R. Draper, *Chemical Science*, 2019, **10**, 7801-7806.
19. X. Du, J. Zhou, J. Shi and B. Xu, *Chemical Reviews*, 2015, **115**, 13165-13307.
20. E. R. Draper and D. J. Adams, *Langmuir*, 2019, **35**, 6506-6521.
21. S. Fleming and R. V. Ulijn, *Chemical Society Reviews*, 2014, **43**, 8150-8177.
22. A. D. Martin and P. Thordarson, *Journal of Materials Chemistry B*, 2020, **8**, 863-877.
23. R. Das, B. Gayakvad, S. D. Shinde, J. Rani, A. Jain and B. Sahu, *ACS Applied Bio Materials*, 2020, **3**, 5474-5499.
24. G. Fichman and E. Gazit, *Acta Biomaterialia*, 2014, **10**, 1671-1682.
25. C. Tomasini and N. Castellucci, *Chemical Society Reviews*, 2013, **42**, 156-172.
26. Z. Yang, G. Liang, M. Ma, Y. Gao and B. Xu, *Journal of Materials Chemistry*, 2007, **17**, 850-854.
27. L. Wang, X. Jin, L. Ye, A.-y. Zhang, D. Bezuidenhout and Z.-g. Feng, *Langmuir*, 2017, **33**, 13821-13827.
28. A. Z. Cardoso, L. L. Mears, B. N. Cattoz, P. C. Griffiths, R. Schweins and D. J. Adams, *Soft Matter*, 2016, **12**, 3612-3621.
29. A. D. Martin, J. P. Wojciechowski, A. B. Robinson, C. Heu, C. J. Garvey, J. Ratcliffe, L. J.

-
- Waddington, J. Gardiner and P. Thordarson, *Scientific Reports*, 2017, **7**, 1-6.
30. L. Chen, K. Morris, A. Laybourn, D. Elias, M. R. Hicks, A. Rodger, L. Serpell and D. J. Adams, *Langmuir*, 2010, **26**, 5232-5242.
31. B. Ozbas, J. Kretsinger, K. Rajagopal, J. P. Schneider and D. J. Pochan, *Macromolecules*, 2004, **37**, 7331-7337.
32. Z. Yang, G. Liang and B. Xu, *Accounts of Chemical Research*, 2008, **41**, 315-326.
33. R. Huang, Y. Wang, W. Qi, R. Su and Z. He, *Materials Letters*, 2014, **128**, 216-219.
34. F. Trausel, F. Versluis, C. Maity, J. M. Poolman, M. Lovrak, J. H. Van Esch and R. Eelkema, *Accounts of Chemical Research*, 2016, **49**, 1440-1447.
35. K. McAulay, P. A. Ucha, H. Wang, A. M. Fuentes-Caparrós, L. Thomson, O. Maklad, N. Khunti, N. Cowieson, M. Wallace and H. Cui, *Chemical Communications*, 2020, **56**, 4094-4097.
36. C. Liu, Y. Wang, Y. Gao, Y. Zhang, L. Zhao, B. Xu and L. S. Romsted, *Physical Chemistry Chemical Physics*, 2019, **21**, 8633-8644.
37. R. Sihombing and W. P. Suwarso, *Makara Journal of Science*, 2012, 51-57.
38. G. Picci, M. T. Mulvee, C. Caltagirone, V. Lippolis, A. Frontera, R. M. Gomila and J. W. Steed, *Molecules*, 2022, **27**, 1257.
39. Y. Lan, M. Corradini, a. G. Weiss, S. Raghavan and M. Rogers, *Chemical Society Reviews*, 2015, **44**, 6035-6058.
40. M. Durell, J. E. Macdonald, D. Trolley, A. Wehrum, P. Jukes, R. Jones, C. Walker and S. Brown, *EPL (Europhysics Letters)*, 2002, **58**, 844.
41. Z. Y. Zhang, J. Zhao J. X., *Synthesis Technology and Application*, 2012, **27**, 1-3+17.
42. D. J. Cornwell, B. O. Okesola and D. K. Smith, *Angewandte Chemie*, 2014, **126**, 12669-12673.
43. L. L. Mears, E. R. Draper, A. M. Castilla, H. Su, B. Dietrich, M. C. Nolan, G. N. Smith, J. Douth, S. Rogers and R. Akhtar, *Biomacromolecules*, 2017, **18**, 3531-3540.
44. F. Tosi, J. A. Berrocal, M. C. Stuart, S. J. Wezenberg and B. L. Feringa, *Chemistry–A European Journal*, 2021, **27**, 326-330.
45. M. J. Hollamby, *Physical Chemistry Chemical Physics*, 2013, **15**, 10566-10579.
46. W. Xuan, L. Xiaoxu, Y. Jinghua, Z. Hong and L. Qingquan, The 13th National Conference on Engineering Dielectrics, Xi'an, Shaanxi, China, 2011.
47. F. Wuerthner, C. Bauer, V. Stepanenko and S. Yagai, *Advanced Materials*, 2008, **20**, 1695-1698.
48. D. Jose, S. Mildred, R. Mary Sebastian and S. Xavier, *IOP conference series. Materials Science and Engineering*, 2022, **1221**, 12036.
49. P. Verma, A. Singh and T. K. Maji, *Chemical Science*, 2021, **12**, 2674-2682.
50. B. Larson, S. Gillmor, J. Braun, L. Cruz-Barba, D. Savage, F. Denes and M. Lagally, *Langmuir*, 2013, **29**, 12990-12996.
51. J. Dinic, L. N. Jimenez and V. Sharma, *Lab on a Chip*, 2017, **17**, 460-473.
52. S. Zhang, M. A. Greenfield, A. Mata, L. C. Palmer, R. Bitton, J. R. Mantei, C. Aparicio, M. O. De La Cruz and S. I. Stupp, *Nature Materials*, 2010, **9**, 594-601.
53. D. McDowall, M. Walker, M. Vassalli, M. Cantini, N. Khunti, C. J. C. Edwards-Gayle, N. Cowieson and D. J. Adams, *Chemical Communications*, 2021, **57**, 8782-8785.
54. T. Christoff-Tempesta, Y. Cho, D.-Y. Kim, M. Geri, G. Lamour, A. J. Lew, X. Zuo, W. R. Lindemann and J. H. Ortony, *Nature Nanotechnology*, 2021, **16**, 447-454.
55. B. D. Wall, S. R. Diegelmann, S. Zhang, T. J. Dawidczyk, W. L. Wilson, H. E. Katz, H. Q. Mao and J. D. Tovar, *Advanced Materials*, 2011, **23**, 5009-5014.
56. S. R. Diegelmann, N. Hartman, N. Markovic and J. D. Tovar, *Journal of the American Chemical Society*, 2012, **134**, 2028-2031.
57. M. Antonietti and S. Förster, *Advanced Materials*, 2003, **15**, 1323-1333.
58. T. Kunitake, Y. Okahata, M. Shimomura, S. Yasunami and K. Takarabe, *Journal of the*

-
- American Chemical Society*, 1981, **103**, 5401-5413.
59. J.-H. Fuhrhop and T. Wang, *Chemical Reviews*, 2004, **104**, 2901-2938.
60. T. Shimizu, R. Iwaura, M. Masuda, T. Hanada and K. Yase, *Journal of the American Chemical Society*, 2001, **123**, 5947-5955.
61. R. Iwaura, K. Yoshida, M. Masuda, M. Ohnishi-Kameyama, M. Yoshida and T. Shimizu, *Angewandte Chemie International Edition*, 2003, **42**, 1009-1012.
62. T. Shimizu and M. Masuda, *Journal of the American Chemical Society*, 1997, **119**, 2812-2818.
63. M. Kogiso, S. Ohnishi, K. Yase, M. Masuda and T. Shimizu, *Langmuir*, 1998, **14**, 4978-4986.
64. R. Akhtar, E. R. Draper, D. J. Adams and J. Hay, *Journal of Materials Research*, 2018, **33**, 873-883.
65. S. Panja, B. Dietrich, A. Trabold, A. Zydel, A. Qadir and D. J. Adams, *Chemical Communications*, 2021, **57**, 7898-7901.
66. J. Dinic, Y. Zhang, L. N. Jimenez and V. Sharma, *ACS macro letters*, 2015, **4**, 804-808.
67. Y. Son, C. Kim, D. H. Yang and D. J. Ahn, *Langmuir*, 2008, **24**, 2900-2907.
68. Y. Li and J. E. Sprittles, *Journal of Fluid Mechanics*, 2016, **797**, 29-59.
69. V. Entov and E. Hinch, *Journal of Non-Newtonian Fluid Mechanics*, 1997, **72**, 31-53.
70. C. A. Dreiss, *Soft Matter*, 2007, **3**, 956-970.
71. R. Huang, D. McDowall, H. Ng, L. Thomson, Y. K. Al-Hilaly, J. Douth, S. Burholt, L. Serpell, R. Poole and D. Adams, *Chemical Communications*, 2022, **58** 10388-10391.
72. J. Dinic, Y. Zhang, L. Jimenez and V. Sharma, Editon edn., 2015.
73. R. Omidvar, S. Wu and H. Mohammadigoushki, *Journal of Rheology*, 2019, **63**, 33-44.
74. E. R. Draper, B. Dietrich, K. McAulay, C. Brasnett, H. Abdizadeh, I. Patmanidis, S. J. Marrink, H. Su, H. Cui and R. Schweins, *Matter*, 2020, **2**, 764-778.
75. P.-G. De Gennes and P.-G. Gennes, *Scaling concepts in polymer physics*, Cornell university press, 1979.
76. F.-X. Simon, T. T. T. Nguyen, N. Díaz, M. Schmutz, B. Demé, J. Jestin, J. Combet and P. J. Mésini, *Soft Matter*, 2013, **9**, 8483-8493.